Article

Autophagy regulates neuronal excitability by controlling cAMP/protein kinase A signaling at the synapse

Melina Overhoff[1] iD, Frederik Tellkamp[1,2] iD, Simon Hess[1,3] iD, Marianna Tolve[1,4] iD, Janine Tutas[1], Marcel Faerfers[1], Lotte Ickert[1,4], Milad Mohammadi[1] iD, Elodie De Bruyckere[1], Emmanouela Kallergi[5], Andrea Delle Vedove[6] iD, Vassiliki Nikoletopoulou[5], Brunhilde Wirth[2,6] iD, Joerg Isensee[7], Tim Hucho[7] iD, Dmytro Puchkov[8] iD, Dirk Isbrandt[9,10] iD, Marcus Krueger[1,2], Peter Kloppenburg[1,3] iD & Natalia L Kononenko[1,4,*] iD

Abstract

Autophagy provides nutrients during starvation and eliminates detrimental cellular components. However, accumulating evidence indicates that autophagy is not merely a housekeeping process. Here, by combining mouse models of neuron-specific ATG5 deficiency in either excitatory or inhibitory neurons with quantitative proteomics, high-content microscopy, and live-imaging approaches, we show that autophagy protein ATG5 functions in neurons to regulate cAMP-dependent protein kinase A (PKA)-mediated phosphorylation of a synapse-confined proteome. This function of ATG5 is independent of bulk turnover of synaptic proteins and requires the targeting of PKA inhibitory R1 subunits to autophagosomes. Neuronal loss of ATG5 causes synaptic accumulation of PKA-R1, which sequesters the PKA catalytic subunit and diminishes cAMP/PKA-dependent phosphorylation of postsynaptic cytoskeletal proteins that mediate AMPAR trafficking. Furthermore, ATG5 deletion in glutamatergic neurons augments AMPAR-dependent excitatory neurotransmission and causes the appearance of spontaneous recurrent seizures in mice. Our findings identify a novel role of autophagy in regulating PKA signaling at glutamatergic synapses and suggest the PKA as a target for restoration of synaptic function in neurodegenerative conditions with autophagy dysfunction.

Introduction

Autophagy is an evolutionarily conserved catabolic process that serves to provide nutrients during starvation and to eliminate defective proteins and organelles through lysosomal degradation (Dikic & Elazar, 2018). The most common form of autophagy is macroautophagy (hereafter autophagy). During this process, parts of the cytoplasm are enclosed in double-membrane vesicles called autophagosomes. These undergo subsequent maturation steps before being delivered to the lysosomes for degradation. The core autophagy machinery includes a component of ubiquitin (Ub)-like conjugation machinery ATG5 (Dikic & Elazar, 2018). During the initial steps of autophagy, the Ub-like protein ATG12 conjugates with ATG5 (ATG12~ATG5), which further establishes a complex with ATG16L1. The ATG5 complex is then recruited to the autophagy initiation site, where it catalyzes the conjugation of LC3 to phosphatidylethanolamine, an event required for autophagosome elongation and closure.

Although nutrient starvation is the most common signal for autophagy induction in several model organisms, including mice (Mizushima *et al*, 2004), starvation protocols involving nutrient deprivation have little effect on the rate of autophagosome formation in neurons (Tsvetkov

1 Cologne Excellence Cluster Cellular Stress Response in Aging-Associated Diseases (CECAD), University of Cologne, Cologne, Germany
2 Faculty of Mathematics and Natural Sciences, Institute of Genetics, University of Cologne, Cologne, Germany
3 Faculty of Mathematics and Natural Sciences, Institute of Zoology, University of Cologne, Cologne, Germany
4 Center for Physiology and Pathophysiology, Faculty of Medicine and University Hospital Cologne, University of Cologne, Cologne, Germany
5 Département des Neurosciences Fondamentales, University of Lausanne, Lausanne, Switzerland
6 Institute of Human Genetics, Center for Molecular Medicine Cologne, Center for Rare Diseases Cologne, Faculty of Medicine and University Hospital Cologne, University of Cologne, Cologne, Germany
7 Translational Pain Research, Department of Anaesthesiology and Intensive Care Medicine, Faculty of Medicine and University Hospital Cologne, University of Cologne, Cologne, Germany
8 Leibniz Institute for Molecular Pharmacology (FMP), Berlin, Germany
9 Institute for Molecular and Behavioral Neuroscience, Faculty of Medicine and University Hospital Cologne, University of Cologne, Cologne, Germany
10 Experimental Neurophysiology, German Center for Neurodegenerative Diseases, Bonn, Germany
*Corresponding author. Tel: +49 221 47884302; E-mail: n.kononenko@uni-koeln.de

et al, 2009; Young et al, 2009; Lee et al, 2011; Maday & Holzbaur Erika, 2014; Maday & Holzbaur, 2016). In fact, it is the selective role of autophagy in eliminating toxic proteins, and dysfunctional organelles that are currently thought to play a major neuroprotective role (Scrivo et al, 2018). Degradative cargo of selective autophagy in neurons includes, among others, several pre- and postsynaptic proteins (Shehata et al, 2012; Lüningschrör et al, 2017; Okerlund et al, 2018; Hoffmann et al, 2019; Hoffmann-Conaway et al, 2020; Shen et al, 2020a; Compans et al, 2021), axonal ER (Kuijpers et al, 2021), and mitochondria (Ashrafi et al, 2014; Han et al, 2020). Such housekeeping function of neuronal autophagy is crucial for the turnover of damaged and/or dysfunctional synaptic proteins and organelles and is required to maintain the pool of functional synaptic vesicles (SV) (Hernandez et al, 2012; Hoffmann et al, 2019) and/or presynaptic Ca^{2+} homeostasis (Kuijpers et al, 2021). Alterations in autophagy protein function have been identified in several neurodegenerative diseases characterized by protein inclusion formation, whereas knock-out (KO) of numerous ATG genes in neuronal progenitors and/or in cerebellar Purkinje neurons leads to severe neurodegeneration accompanied by dramatic accumulation of ubiquitinated protein aggregates (reviewed in Overhoff et al, 2021). However, accumulating evidence indicates that neuronal autophagy is not merely a housekeeping process. Neurons utilize components of the autophagy machinery to regulate neurotrophic signaling (Kononenko et al, 2017; Andres-Alonso et al, 2019) and microtubule dynamics (Negrete-Hurtado et al, 2020). Autophagy is also crucial for synapse assembly and pruning (Shen & Ganetzky, 2009; Tang et al, 2014; Stavoe Andrea et al, 2016; Kiral et al, 2020) and required for synaptic plasticity and memory formation (Bhukel et al, 2019; Glatigny et al, 2019; Shen et al, 2020a; Compans et al, 2021; Pandey et al, 2021). How precisely autophagy contributes to synaptic function is currently under debate.

Here we describe that autophagy can regulate synaptic function independently of its role in the turnover of damaged proteins and organelles. By using neuronal-confined mouse models of ATG5 deficiency in either excitatory or inhibitory neurons and a combination of SILAC and label-free quantitative proteomics, high-content microscopy, and live-imaging approaches, we show that autophagy functions in neurons to mediate turnover of the synapse-localized regulatory R1α and R1β subunits of protein kinase A (PKA). Loss of ATG5 in neurons is accompanied by sequestration of the PKA catalytic subunit by its inhibitory R1α/β subunits, which diminishes PKA signaling and causes cAMP-dependent remodeling of the cytoskeletal phosphoproteome confined to the postsynaptic density of excitatory synapses. Autophagy-deficient synapses are characterized by increased postsynaptic density thickness (PSD), impaired trafficking of AMPA receptors, and enhanced excitatory neurotransmission, a PKA-dependent phenotype that coincides with the occurrence of seizures in mice with glutamatergic forebrain-confined ATG5 deletion. Our results point to a previously unknown role for autophagy in regulating PKA signaling in the brain, where it acts as a modulator of synaptic activity in cortical excitatory neurons.

Results

ATG5 deficiency in excitatory neurons results in the appearance of spontaneous seizures

To understand how precisely autophagy contributes to neuronal function, we capitalized on two mouse lines lacking crucial autophagy component ATG5 either in forebrain excitatory (Atg5flox:flox/CamKIIα-Cre[tg] KO mice, further defined as Atg5flox:CamKIIα-Cre KO, Fig 1A and B) or inhibitory (Atg5flox:flox/Slc32a1-Cre[tg] KO mice, further defined as Atg5flox:Slc32a1-Cre KO, Fig 1C and D) neurons. For our studies, we exploited the fact that the majority of neurons in the cortex are glutamatergic, while the majority of neurons in the striatum are GABAergic. Therefore, cortical lysates were used to analyze the effect of autophagy deficiency on excitatory neurons in Atg5flox:CamKIIα-Cre KO mice, whereas striatal tissue was used the measure alterations in GABAergic neurons in Atg5flox:Slc32a1-Cre KO mice. Similar to previously published Atg5flox:CamKIIα-Cre KO mice (Negrete-Hurtado et al, 2020), Atg5flox:Slc32a1-Cre KO mice were viable but revealed a cessation of weight gain starting at about 1 month of age when compared to their WT littermates (Appendix Fig S1A). Autophagy inhibition in Atg5flox:CamKIIα-Cre KO and Atg5flox:Slc32a1-Cre KO brains was reflected by significantly increased protein levels of autophagy receptor p62 (Fig 1E–H) and downregulated levels of LC3 at autophagosomal membranes (monitored via LC3II levels, Appendix Fig S1B). In line with the absence of neurodegeneration in mice lacking ATG5 in a CamKIIα-dependent manner (Negrete-Hurtado et al, 2020), we detected no loss of GABAergic neurons in the hippocampus and entorhinal cortex of 3-month-old Atg5flox:Slc32a1-Cre KO mice (Appendix Fig S1C–E), a phenotype that was consistent until 10 months of age (Appendix Fig S1F and G).

Autophagy has previously been shown to promote memory formation (Glatigny et al, 2019). To further characterize the effects of neuronal ATG5 deletion on mouse behavior, we employed the SmithKline, Harwell, Imperial College, Royal Hospital, Phenotype Assessment (SHIRPA)-based test battery, which includes 22 measures of motor activity, postural control, emotional reactivity, and visual and auditory reflexes (Lalonde et al, 2021). We found that although mice lacking ATG5 in either excitatory or inhibitory neurons exhibited only minor neurological abnormalities (Appendix Fig S1H and I), both the Atg5flox:CamKIIα-Cre and Atg5flox:Slc32a1-Cre KO lines responded with potentiated startle reflex to stimulus presentation compared to their control littermates (i.e. either Atg5wt:wt/Slc32a1-Cre[tg], Atg5flox:wt/Slc32a1-Cre[wt] or Atg5flox:flox/Slc32a1-Cre[wt], further defined as Atg5flox:Slc32a1-Cre WT, and Atg5flox:wt/CamKIIα-Cre[wt] or Atg5flox:flox/ CamKIIα-Cre[wt], further defined as Atg5flox:CamKIIα-Cre WT, see also Material and Methods for definition of genotypes; Fig 1I and J). However, only a significant percentage of Atg5flox:CamKIIα-Cre KO mice showed epileptic behavioral seizures when exposed to loud noise (Fig 1K and L; Movie EV1). The seizures were present in 62% of homozygous 10-week-old Atg5flox/flox:CamKIIα-Cre mice and in 19% of heterozygous 22-week-old Atg5flox/wt:CamKIIα-Cre mice. The presence of pathological electrocorticogram (ECoG) patterns, such as interictal spikes, spike trains, and spontaneous unprovoked electrographic generalized tonic–clonic seizures were documented in chronic radiotelemetry recordings from the somatomotor cortical region of 12-week-old Atg5flox/flox:CamKIIα-Cre KO mice indicative of their increased neuronal network hyperexcitability (Fig 1M and N, see also Appendix Fig S2 for REM, SWS, and active awake periods in WT and KO animals). Interestingly, although behavioral seizures did not occur in 10–13 week-old Atg5flox:Slc32a1-Cre KO mice (Fig 1L), they were evident in a small percentage of animals (< 4%) at 10 month of age and older (Appendix Fig S1J).
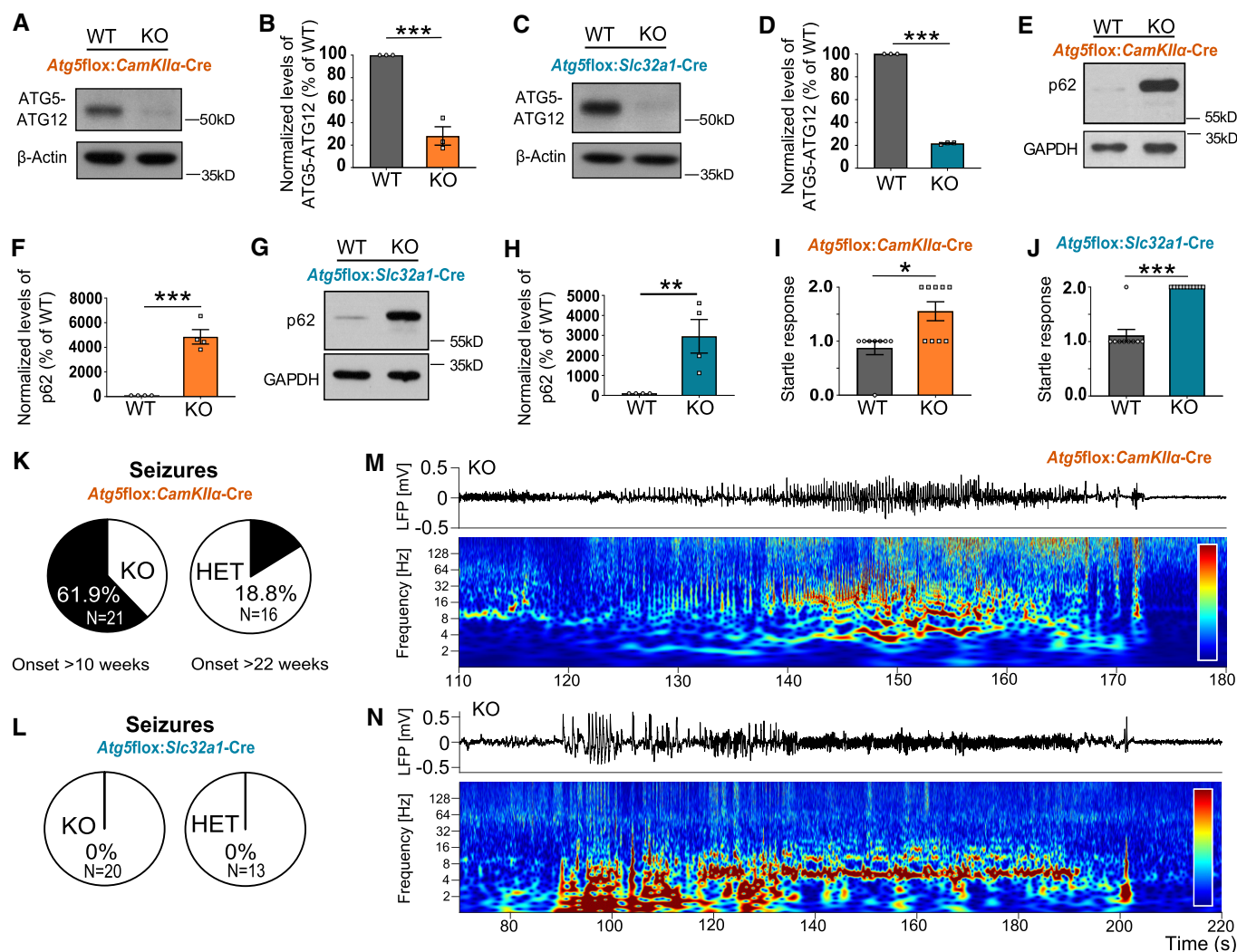
Figure 1. ATG5 deficiency in excitatory and inhibitory neurons results in differential neuronal excitability.

A, B   Immunoblot analysis of ATG5-ATG12 protein levels in cortical brain lysates of 13-week-old *Atg5*flox:*CamKIIα*-Cre WT/KO mice (WT set to 100%, KO: 28.13 ± 8.18%; $P = 0.0005$, $n_{WT} = 3$, $n_{KO} = 3$, one-tailed unpaired t-test).

C, D   Immunoblot analysis of ATG5-ATG12 protein level in striatal brain lysates of 13-week-old *Atg5*flox:*Slc32a1*-Cre WT/KO mice ($P < 0.0001$, $n_{WT} = 3$, $n_{KO} = 3$, one-tailed unpaired t-test).

E, F   Protein levels of p62 are significantly increased in cortical lysates of *Atg5*flox:*CamKIIα*-Cre KO mice compared to the WT set to 100% (KO: 4,855 ± 587.4%; $P < 0.0001$, $n = 4$, one-tailed unpaired t-test).

G, H   Protein levels of p62 are significantly increased in striatal lysates of *Atg5*flox:*Slc32a1*-Cre KO mice compared to the WT set to 100% (KO: 2956 ± 839.3%; $P = 0.0072$, $n = 4$, one-tailed unpaired t-test).

I, J   Startle response analysis of *Atg5*flox:*CamKIIα*-Cre WT/KO mice (I) (WT: 0.88 ± 0.125, KO: 1.56 ± 0.176; $P = 0.0204$, $n_{WT} = 8$, $n_{KO} = 9$) and *Atg5*flox:*Slc32a1*-Cre WT/KO mice (J) (WT: 1.11 ± 0.111, KO: 2.00 ± 0.000; $P < 0.0001$, $n_{WT} = 9$, $n_{KO} = 11$, two-tailed Mann–Whitney test).

K, L   Behavioral seizure analysis in *Atg5*flox:*CamKIIα*-Cre KO and heterozygous (HET) mice (K), as well as in *Atg5*flox:*Slc32a1*-Cre KO/HET mice (L). Mice were observed twice a week during 4 months after birth (the number animals and the age of seizure onset are indicated in the graph). No seizures were detected in WT mice.

M, N   Examples of electrocorticogram (ECoG) traces (top) and corresponding wavelet spectrograms (bottom, warm colors indicate high power) from *Atg5*flox:*CamKIIα*-Cre KO mice during a spontaneous generalized tonic–clonic seizure (M), or during a focal seizure associated with repetitive grooming and head-nodding (N). Representative example from $n = 4$ recordings for each genotype. All data represent mean ± SEM.

Data information: *$P < 0.05$; **$P < 0.01$; ***$P < 0.001$. All data represent mean ± SEM. All n represent biological replicates.
Source data are available online for this figure.

PKA R1α/β levels are highly upregulated in autophagy-deficient excitatory and inhibitory neurons *in-vivo*

How does neuronal ATG5 prevent the onset of seizures in mice? A recent study in mice lacking ATG5 in EMX1-lineage progenitors suggested that ATG5 regulates neurotransmission by selectively degrading the components of presynaptic tubular ER, although these mice were not reported to develop seizures (Kuijpers *et al*, 2021). Another study proposed that autophagy could regulate neuronal excitability by governing the degradation of damaged SV proteins

(Hoffmann *et al*, 2019). To reveal whether the changes in axonal ER components and/or bulk synaptic proteome are reflected in brains conditionally lacking ATG5 in either excitatory or inhibitory neurons, we conducted quantitative proteomics studies. First, we performed global proteomic profiling of conditional ATG5 KO mice using a spike-in SILAC mouse approach, where heavy SILAC reference brain tissue (Krüger *et al*, 2008) was spiked into brain lysates obtained from either 12–13-week-old *Atg5*flox:*CamKIIα*-Cre (cortex) and *Atg5*flox:*Slc32a1*-Cre (striatum) KO mice or their control littermates (Appendix Fig S3A). In agreement with Kuijpers *et al* (2021) we found no major alterations in bulk levels of SV proteins in brains lacking ATG5 in either excitatory or inhibitory neurons (see also Appendix Fig S5C and D). In fact, except for known autophagy receptors such as GABARAPL2 and p62 (SQSTM1), only a few proteins were highly upregulated at the significance levels of $P < 0.05$ and log2 fold change of > 1 (Fig 2A), and these changes were only slightly intensified at log2 fold change of > 0.5 (Appendix Fig S3B). Among highly upregulated proteins in *Atg5*flox:*Slc32a1*-Cre KO brains we detected recently identified reticulophagy receptors TEX264 and SEC62, implicating reticulophagy in maintaining the physiology of forebrain inhibitory neurons (Fig 2B). Intriguingly, in both types of autophagy-deficient neurons, regulatory subunits of protein kinase A (PKA) holoenzyme R1α (PRKAR1A) and R1β (PRKAR1B) were the most significantly upregulated proteins. These findings provided the first line of evidence that autophagy may regulate PKA signaling in excitatory and inhibitory neurons.

To understand whether the changes in brain PKA R1α and R1β levels described above are due to a cell-autonomous role of autophagy in neurons, we developed a fluorescence-activated cell sorting (FACS)-based strategy to perform label-free proteomic analyses of WT and ATG5 KO neurons. We isolated neurons from brains of 3–4 week-old (the age at which the contribution of debris to cell sorting is relatively low) *Atg5*flox:*CamKIIα*-Cre (cortex) and *Atg5*flox:*Slc32a1*-Cre (striatum) WT and KO mice that additionally carried the tdTomato allele (*Ai9*) (Appendix Fig S3C). ATG5 levels were significantly decreased in FACS-sorted *Atg5*flox:*CamKIIα*-Cre:*Ai9* KO neurons and completely undetectable in neurons isolated from *Atg5*flox:*Slc32a1*-Cre:*Ai9* KO mice (Fig 2C and D; Dataset EV1), reflecting the reliability of our FACS-sorting protocol. Protein classification analysis revealed that most of the proteins enriched in the FACS-sorted KO neurons *in-vivo* belonged to metabolite interconversion enzymes, nucleic acid metabolism proteins and/or protein-modifying enzymes (Appendix Fig S3D and E). In agreement with the data from SILAC-based proteomics, PKA R1α and R1β subunits were among the significantly upregulated proteins in FACS-sorted ATG5-deficient neurons. This upregulation was less robust in ATG5 KO excitatory neurons, likely reflecting PKA R1α/β confinement to peripheral synaptic processes (see also Fig 3), which cannot be detected in the FACS-based proteomics approach. We next subjected proteins identified in FACS-based proteomics in both mouse lines to a Gene Ontology (GO) term enrichment analysis aiming at identifying cellular components and molecular functions, which are cell-autonomously regulated by autophagy in both classes of neurons. GO term analysis of proteome from FACS-sorted autophagy-deficient excitatory and inhibitory neurons revealed an enrichment of several pre- and postsynaptic proteins (e.g., RIMS2, CPLX1, SYP, CNIH2, DAGLB; Fig 2E; see also Dataset EV1). These data agree with several recent studies and highlight the cell-autonomous role

of autophagy in maintaining the homeostasis of synaptic proteins in the soma of excitatory and inhibitory neurons *in-vivo* (Nikoletopoulou *et al*, 2017; Shen *et al*, 2020a; Compans *et al*, 2021; Goldsmith *et al*, 2022). In line with recent work (Goldsmith *et al*, 2022), we were not able to detect enrichment and/or upregulation of mitophagy regulators such as PINK1 or Parkin. This may either reflect the absence of mitochondrial clearance by autophagy in the cell soma of neurons or suggest the existence of ATG5-independent pathways for neuronal mitophagy.

Consistent with the upregulation of PKA R1α and R1β subunits in ATG5-deficient neurons, GO term enrichment analysis revealed "cAMP-dependent PKA complex" (Fig 2E) and PKA-associated pathways (Appendix Fig S3F–H) as top-ranked GO terms. PKA is a key kinase involved in the regulation of multiple cellular transduction pathways. PKA holoenzyme is a heterotetramer consisting of a dimer of two regulatory (R) subunits, each binding a catalytic subunit. PKA signaling is activated when two molecules of cAMP bind each R subunit of PKA heterotetramer, leading to its dissociation and release of the catalytic subunits (Taylor *et al*, 2021). Catalytic subunits then become active to phosphorylate protein substrates at serine or threonine residues, resulting in changes in cell function. Importantly, in the brain, the PKA function is essential in the regulation of synaptic activity, where PKA takes a major role in controlling glutamate receptor and sodium channels function at synapses (Abel & Nguyen, 2008). This established role of PKA in regulating synaptic physiology, together with our findings indicating an increase in protein levels of R1α- and R1β-subunits of the PKA complex in autophagy-deficient neurons, prompted us to further investigate the link between autophagy, PKA signaling, and synaptic function.

Neuronal autophagy regulates synaptic levels of PKA R1α/β subunits

The data described above suggest that autophagy regulates the protein levels of the inhibitory subunits of the PKA holoenzyme R1α and R1β in excitatory and inhibitory neurons. To further test this hypothesis, we first validated the results from the proteomics studies by Western Blotting. The levels of R1α and R1β were upregulated in the cortex and hippocampus of 12–13-week-old *Atg5*flox:*CamKIIα*-Cre KO mice (Fig 2F and G; Appendix Fig S4A and B), as well as in the striatum and cortex of 12–13-week-old *Atg5*flox:*Slc32a1*-Cre KO mice (Fig 2H and I; Appendix Fig S4C). In mammals, four inhibitory R subunits (R1α, R1β, R2α, and R2β) have been identified, comprising the type 1 or the type 2 PKA isozymes, respectively (Taylor *et al*, 2021). Since all four R subunits are expressed in the brain, we investigated the levels of R2α and R2β in brain lysates of autophagy-deficient mice. The levels of R2α and R2β were neither altered in the brains of *Atg5*flox:*CamKIIα*-Cre KO mice (Appendix Fig S4D and E), nor in brains of *Atg5*flox:*Slc32a1*-Cre KO mice (Appendix Fig S4F). Furthermore, ATG5 was also dispensable for the regulation of neuronal levels of the catalytic PKA-Cα subunit (Appendix Fig S4G–I). In addition, the levels of R1α and R1β, but not PKA-Cα, were also dysregulated in the *in-vitro* cortico-hippocampal culture system, where the deletion of ATG5 (Appendix Fig S4J–L) was driven by a tamoxifen-dependent activation of the *CAG*-Cre promoter (Cre^Tmx) (Negrete-Hurtado *et al*, 2020). This effect was not specific to ATG5, as deletion of
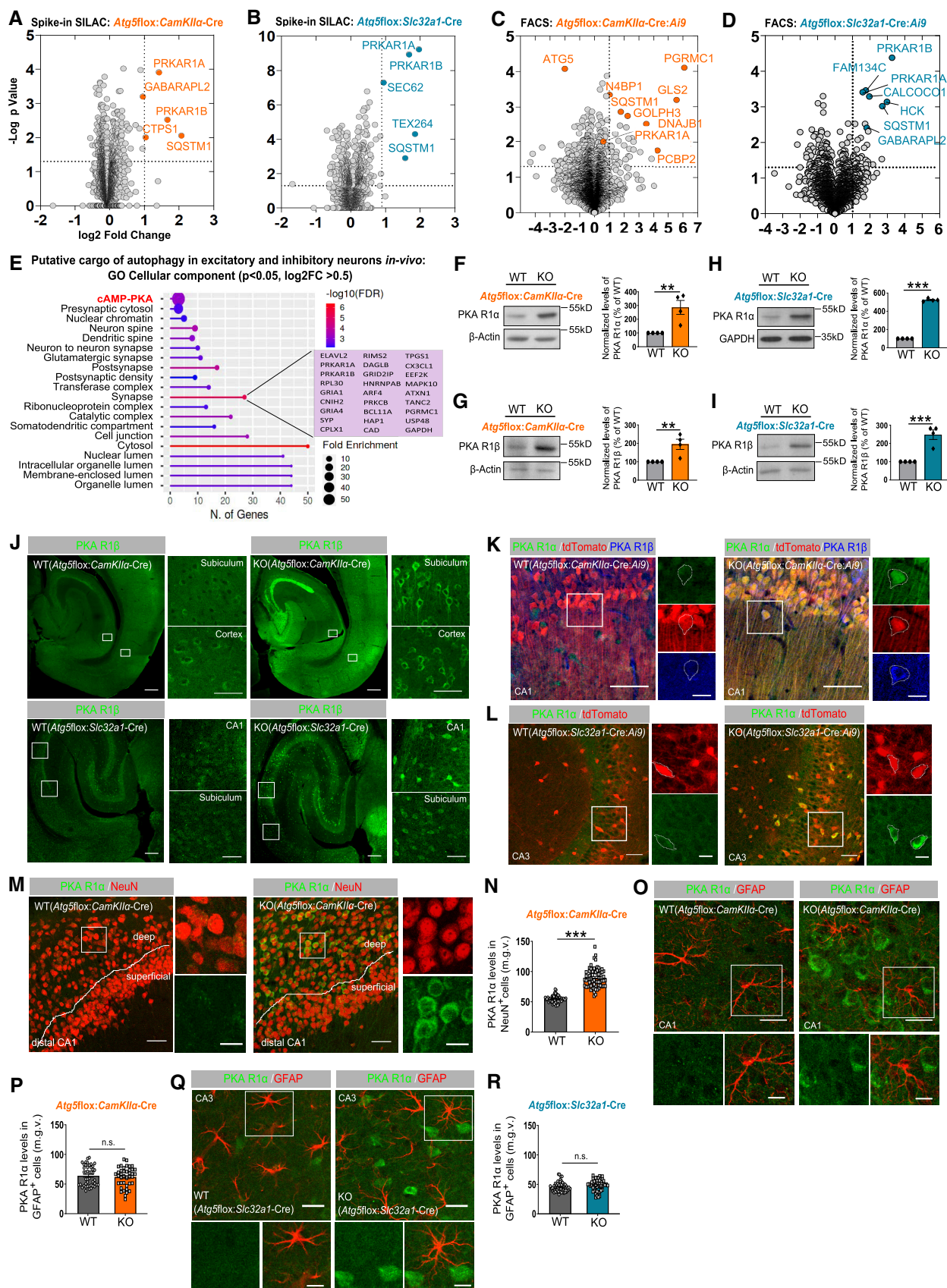
Figure 2.

◄

Figure 2.   PKA R1α/β subunits of the PKA complex are upregulated in autophagy-deficient excitatory and inhibitory neurons *in-vivo*.

A, B   Volcano plot of differentially expressed proteins in *Atg5*flox:*CamKIIα*-Cre KO cortical brain lysates (A) and *Atg5*flox:*Slc32a1*-Cre KO striatal brain lysates (B), analyzed using a SILAC-based proteomic approach ($n_{Atg5flox:CamKIIα-Cre}$ = 3, $n_{Atg5flox:Slc32a1-Cre}$ = 5 mice per genotype). Orange- and blue-color-coded circles indicate all protein deregulated at $P < 0.05$ and log2 fold change of > 1.

C, D   Volcano plot of differentially expressed proteins in FACS-sorted *Atg5*flox:*CamKIIα*-Cre:*Ai9* (C) and *Atg5*flox:*Slc32a1*-Cre:*Ai9* (D) KO neurons, analyzed using label-free proteomic analysis ($n_{Atg5flox:CamKIIα-Cre:Ai9}$ = 4, $n_{Atg5flox:Slc32a1-Cre:Ai9}$ = 5 mice per genotype). Orange- and blue-color-coded circles highlight highly deregulated proteins at $P < 0.05$ and log2 fold change of > 1. See also Dataset EV1.

E   ShinyGO v0.741-based GO analysis of "cellular component" -enriched terms in the proteome (cut-off $P < 0.05$, log2FC > 0.5) of FACS sorted *Atg5*flox:*CamKIIα*-Cre:*Ai9* KO and *Atg5*flox:*Slc32a1*-Cre:*Ai9* KO neurons.

F, G   PKA R1α (F) and PKA R1β (G) protein levels are significantly increased in cortical brain lysates from 13-week-old *Atg5*flox:*CamKIIα*-Cre KO mice compared to the WT set to 100% (KO$_{PKA R1α}$: 286.1 ± 50.53%, $P = 0.005$, KO$_{PKA R1β}$: 194.7 ± 27.82%, $P = 0.007$, one-tailed unpaired *t*-test). $n = 4$ for each genotype.

H, I   PKA R1α (H) and PKA R1β (I) protein levels are significantly increased in striatal lysates of *Atg5*flox:*Slc32a1*-Cre KO mice compared to the WT set to 100% (KO$_{PKA R1α}$: 524.1 ± 8.35%, $P < 0.0001$, KO$_{PKA R1β}$: 247.9 ± 26.26%, $P = 0.0007$, one-tailed unpaired *t*-test). $n = 4$ for each genotype.

J   Immunohistochemistry for PKA R1β on horizontal brain sections from *Atg5*flox:*CamKIIα*-Cre WT/KO and *Atg5*flox:*Slc32a1*-Cre WT/KO mice. White rectangular boxes indicate areas magnified to the right. Scale bars: 200 μM in large panels, 50 μM in small panels.

K, L   Immunohistochemistry for PKA R1β and PKA R1α on horizontal brain sections from *Atg5*flox:*CamKIIα*-Cre:*Ai9* (K) and *Atg5*flox:*Slc32a1*-Cre:*Ai9* WT/KO (L) mice. White rectangular boxes indicate areas magnified to the right. Scale bars: 50 μm, 25 μm (small panels in K), 20 μm (small panels in L). Drawn contours indicate representative WT or KO neuronal cell body.

M, N   Immunohistochemistry analysis of PKA R1α levels in NeuN-posititve neurons in the hippocampus of *Atg5*flox:*CamKIIα*-Cre WT/KO mice. Scale bar: 50 μm, 20 μm (small panels). WT: 54.70 ± 0.693, KO: 89.79 ± 1.831; $P < 0.0001$, two-tailed unpaired *t*-test. n_{WT} = 64; n_{KO} = 71 neurons from $n = 3$ mice per genotype.

O, P   Immunohistochemistry analysis of PKA R1α levels in GFAP-positive cells in the hippocampus of *Atg5*flox:*CamKIIα*-Cre WT/KO mice. Scale bar: 50 μm, 30 μm (small panels). WT: 63.86 ± 2.477, KO: 61.71 ± 2.653; $P = 0.5549$, two-tailed unpaired *t*-test. n_{WT} = 45; n_{KO} = 40 cells from $n = 3$ mice per genotype.

Q, R   Immunohistochemistry analysis of PKA R1α in GFAP-positive cells in the hippocampus of *Atg5*flox:*Slc32a1*-Cre WT and KO mice. Scale bar: 50 μm, 30 μm (small panels). WT: 45.28 ± 1.018, KO: 48.50 ± 1.440; $P = 0.0636$, two-tailed unpaired *t*-test. n_{WT} = 61; n_{KO} = 48 cells from $n = 3$ mice per genotype.

Data information: *$P < 0.05$; **$P < 0.01$; ***$P < 0.001$. All data represent mean ± SEM. All n represent biological replicates.
Source data are available online for this figure.

ATG16L1, another component of the ATG12~ATG5-ATG16L1 conjugate, was sufficient to stabilize the levels of R1α/β in tamoxifen-treated primary neurons isolated from *Atg16L1*flox:*CAG*-Cre^{Tmx} mice (Appendix Fig S4M), as well as in cortical brain lysates from 12 to 13-week-old *Atg16L1*flox: *Slc32a1*-Cre KO mice (Appendix Fig S4N). Overall, our data suggest that autophagy selectively regulates neuronal levels of type 1 PKA subunits both *in-vivo* and *in-vitro*.

Next, we determined the precise cellular and subcellular localization of R1α and R1β in neurons. To this aim, we first performed immunohistochemical analysis of R1α and R1β in the brains of *Atg5*flox:*CamKIIα*-Cre and *Atg5*flox:*Slc32a1*-Cre WT and KO mice, using R1β antibodies, which recognize R1α in addition, when used for immunohistochemistry (Ilouz *et al*, 2012). R1β was expressed in the hippocampus and the cortex of control mice, and this expression pattern was further enhanced by the ATG5 deletion (Fig 2J). The upregulation of PKA R1α and R1β was specific to KO neurons, as shown by their restriction to tdTomato-expressing neurons in *Atg5*flox:*CamKIIα*-Cre KO and *Atg5*flox:*Slc32a1*-Cre KO mice, carrying the tdTomato allele (*Ai9*) as a reporter (Fig 2K and L). Levels of PKA R1α were also significantly increased in KO neurons positive for the neuronal marker NeuN (Fig 2M and N) but not in cells expressing GFAP (astrocyte marker) and/or MBP (oligodendrocyte marker; Fig 2O–R; Appendix Fig S4O–R).

To understand the localization of PKA R1α/β at the cellular level, we employed the 3D-based reconstruction approach, which revealed R1α accumulation in neuronal soma and neuropil (Fig 3A). PKA R1α/β subunits were found to be significantly more confined to bassoon-positive (Fig 3B–F; Appendix Fig S5A) and PSD95-positive (Fig 3G and H) synapses in *Atg5*flox:*CamKIIα*-Cre KO brains. Although murine R1α and R1β share 82% sequence identity, they are not functionally redundant, which can be partially explained by their differential subcellular localization, where

R1α is cytosolic, whereas R1β is selectively enriched in the mitochondria (Ilouz *et al*, 2012). To reveal the subcellular localization of R1α /β in autophagy-deficient neurons, we performed immunogold-based labeling on Tokuyasu cryosections of the CA1 neuropil area of the hippocampus in *Atg5*flox:*CamKIIα*-Cre WT and KO mice. In agreement with (Ilouz *et al*, 2012), our immunogold analysis revealed a relatively sparse cytoplasmic labeling for R1α in WT neurons and its accumulation in the cytosol of dendrites and at the PSD of neurons, lacking ATG5 (Fig 3I). However, due to the sparse content of R1α antibody labeling in the WT, we were not able to quantify these differences. In contrast, the antibody recognizing both R1α and R1β subunits was efficient in labeling R1α/β subcellular distribution in both WT and ATG5-deficient brains (the specificity of immunogold labeling was confirmed by the complete absence of gold particles in the "negative control" samples). Interestingly, we found that a lack of autophagy led to a significant accumulation of type 1 PKA subunits at synapses and mitochondria (Fig 3J; Appendix Fig S5B). These data, taken together with the fact that no alterations in bulk levels of SV proteins were identified upon neuronal autophagy deficiency in SILAC-based proteomics (Appendix Fig S5C and D), suggest that autophagy might contribute to neuronal function via regulating the PKA-dependent signaling at synapses and/or mitochondria. Since autophagy-mediated degradation of R1α has been recently shown to regulate the mitochondrial metabolism in response to glucose starvation in non-neuronal cells (Deng *et al*, 2021), we focused our further studies on the autophagy-dependent PKA function at synapses.

PKA type 1 subunits are cargo of neuronal autophagy

To understand how precisely autophagy regulates levels of R1α and R1β in neuronal cells, we first tested the effect of starvation and/or
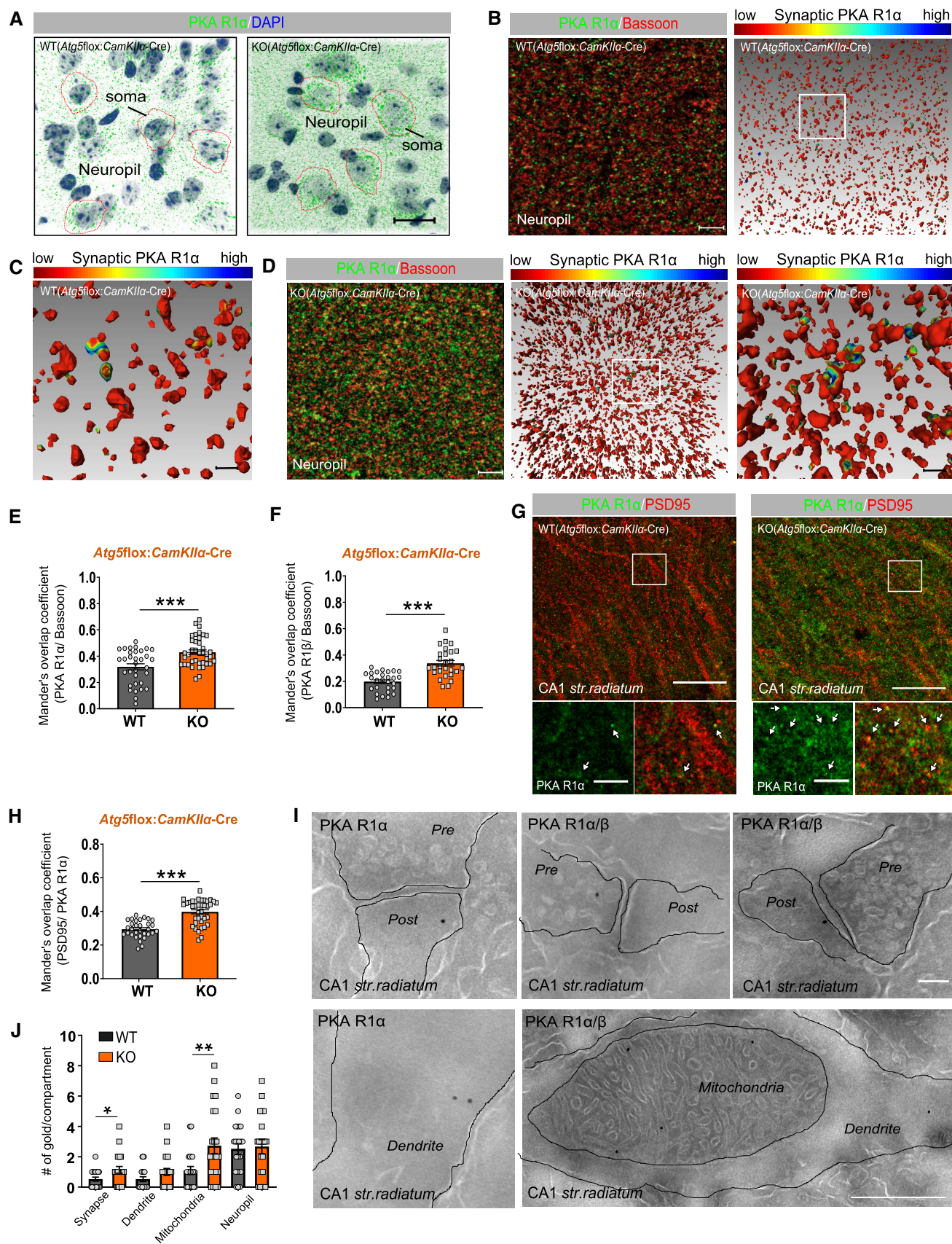
Figure 3.

Figure 3. PKA R1α/β subunits of the PKA complex are enriched at the synaptic compartments of autophagy-deficient neurons.

A   AMIRA-based 3D-visualization of PKA R1α distribution in *Atg5*flox:*CamKIIα*-Cre WT/KO cell soma and neuropil in the cortex. Scale bar 20 μm. Drawn contours indicate somata of WT or KO neurons.

B–D Immunohistochemical analysis and surface rendering of Amira 3D reconstructions of PKA R1α and bassoon colocalization in *Atg5*flox:*CamKIIα*-Cre WT (B, C) and KO (D) cortical neuropil. In 3D analysis, the PKA R1α neuropil staining is represented by 3D reconstruction of its surface in red and PKA R1α/bassoon contacts are color coded, with the cold to warm colors spreading from 0- to 250-nm distance between the surface of either bassoon-positive synapses and/or PKA R1α-positive neuropil (see color-coded horizontal bar for the distance definition). Scale bar 5 μm in dual-channel, 1 μm in 3D-reconstruction zoom.

E   Mander's overlap coefficient of PKA R1α and bassoon colocalization in Atg5flox:CamKIIα-Cre WT/KO cortex (WT: 0.32 ± 0.023, KO: 0.43 ± 0.018; $P = 0.0002$, two-tailed unpaired t-test). $n_{WT} = 33$; $n_{KO} = 39$ from $n = 3$ mice.

F   Mander's overlap coefficient of PKA R1β and bassoon colocalization in *Atg5*flox:*CamKIIα*-Cre WT/KO cortex (WT: 0.20 ± 0.014, KO: 0.34 ± 0.021; $P < 0.0001$, two-tailed unpaired t-test). $n_{WT} = 27$; $n_{KO} = 27$ from $n = 3$ mice (see also Appendix Fig S5A).

G   Immunohistochemistry for PKA R1α and postsynaptic density marker PSD95 on horizontal brains sections from *Atg5*flox:*CamKIIα*-Cre WT/KO mice. White rectangular boxes indicate areas magnified below with arrows indicating PKA R1α and PSD95 colocalization. Scale bar: 20 μm, 5 μm (insert).

H   Mander's overlap coefficient of PKA R1α and PSD95 colocalization in *Atg5*flox:*CamKIIα*-Cre WT/KO hippocampus (WT: 0.29 ± 0.009, KO: 0.40 ± 0.012; $P < 0.0001$, two-tailed unpaired t-test). $n_{WT} = 31$; $n_{KO} = 38$ from $n = 3$ mice.

I   Electron microscopy-based analysis of immunogold-labeled PKA R1α/β on Tokuyasu cryosections of the CA1 neuropil area of the hippocampus of *Atg5*flox:*CamKIIα*-Cre KO mice. No immunogold labelling was detected in samples where the PKA R1α/β antibody were omitted (negative control). Scale bar: upper row 50 nm, 500 nm lower picture. (J) PKA R1α/β is enriched at mitochondria (WT: 1.10 ± 0.266, KO: 2.73 ± 0.515; $P = 0.0082$, two-tailed unpaired t-test) and synapses (WT: 0.52 ± 0.131, KO: 1.14 ± 0.221; $P = 0.0234$, two-tailed unpaired t-test) of KO mice. Values display the mean number of gold particles counted per structure in $n_{WT} = 21$ and $n_{KO} = 22$ pictures per genotype.

Data information: *$P < 0.05$; **$P < 0.01$; ***$P < 0.001$. All data represent mean ± SEM. All n represent biological replicates.
Source data are available online for this figure.

mTORC1 inhibition, two conditions known to induce autophagy, on the levels of PKA R1α in NSC34 cells. We found that PKA R1α levels were significantly decreased in neuronal cells subjected to amino acid and serum starvation using media containing 5 mM glucose (Fig 4A and B; Appendix Fig S6A). Starvation-dependent decrease in PKA R1α was rescued by acute suppression of autophagy using a specific V-ATPase inhibitor Bafilomycin A1 (Fig 4C). In contrast to starvation, the decrease in PKA R1α was not evident upon treatment of NSC34 cells with an ATP-competitive inhibitor of mTOR, Torin1 (Fig 4A), although the levels of pS6 Ser-235/236, used as a readout of mTORC1 activity, were equally decreased (Appendix Fig S6B and C), suggesting that starvation decreases R1α levels independently of mTORC1 activity. Early work in *Aplysia* has established that cAMP levels *per se* are a crucial regulator of PKA R1α/β degradation. High cAMP levels cause dissociation of the holoenzyme, releasing R subunits that are then targeted for ubiquitin-mediated degradation (Chain *et al*, 1999). To test whether starvation regulates PKA R1α/β degradation by increasing cAMP levels, we analyzed cAMP levels in primary cortico-hippocampal neurons starved for 16 h. We found that starvation increases cAMP levels by approximately 20% (Fig 4D and E). This effect was paralleled by increased phosphorylation of PKA substrates, which could be prevented by the application of the ATP-site PKA inhibitor H89 (Fig 4F and G). These data suggest that starvation may initiate PKA R1 degradation via a mTORC1-independent mechanism involving dissociation of the PKA holoenzyme due to elevated cAMP levels.

Are starvation-released PKA R1 subunits degraded in constitutively formed autophagosomes? To answer this question, we first analyzed the PKA R1α levels in NSC34 cells cultured in normal media and treated with Bafilomycin A1 (Fig 4H). PKA R1α was robustly stabilized in Bafilomycin A1-treated cells (Fig 4I), suggesting that basal autophagy may be directly responsible for the R1α degradation. Consistent with this hypothesis, both R1α- and R1β-subunits were found in purified mouse brain autophagosomes (Fig 4J), which indicates that R1α/β subunits of the PKA complex are cargo of neuronal autophagy.

If R1α and R1β are a selective cargo of neuronal autophagosomes, autophagy dysfunction should lead to their accumulation in p62 (SQSTM1)-positive inclusions. In agreement with this hypothesis, we observed confinement of R1α and R1β to p62-containing puncta in the cell soma of neurons of *Atg5*flox:*CamKIIα*-Cre KO mice (Fig 4K; Appendix Fig S6D). The loss of ATG5 in GABAergic neurons also caused the soma-confined accumulation of R1 α/β to inclusion bodies positive for p62 and another selective autophagy receptor NBR1 (Fig 4L; Appendix Fig S6E and F). In the soma of WT neurons, the colocalization of R1α and p62 was regulated by starvation and could be facilitated by autophagy inhibition (Fig 4M and N). Interestingly, in contrast to the cell soma (Fig 4O), the enrichment of R1β at ATG5 deficient synapses was not accompanied by p62 accumulation (Fig 4P; Appendix Fig S6G and H), suggesting that the initial targeting of R1β to synaptic autophagosome membranes does not require the selective autophagy receptor p62 and might be mediated by its interaction with LC3. In agreement with this hypothesis, co-immunoprecipitation analysis revealed biochemical association of R1β with LC3 in the brain (Appendix Fig S6I). Finally, significantly more PKA R1α and R1β was found to be associated with PKA catalytic subunit in brain lysates of *Atg5*flox:*CamKIIα*-Cre KO mice (Fig 4Q and R). Overall, these results show that basal autophagy regulates PKA R1 protein levels in neurons and its loss stabilizes synaptic R1α and R1β levels, ultimately leading to sequestration of the catalytic PKA subunit.

ATG5 regulates the cAMP/PKA/CREB1 signaling axis in the brain

A prediction from the data described above is that upregulated levels of PKA R1 subunits in neurons with ATG5 deletion (without compensation of PKA-Cα levels, see Appendix Fig S4G–I) diminish PKA signaling. PKA activity is tightly controlled by cAMP and can be enhanced by the addition of the cAMP-elevating agent forskolin, resulting in the phosphorylation of CREB (pCREB) at Ser 133. As shown in Fig 5A, CREB phosphorylation was increased in primary WT cortico-hippocampal neurons treated with 10 μM forskolin for
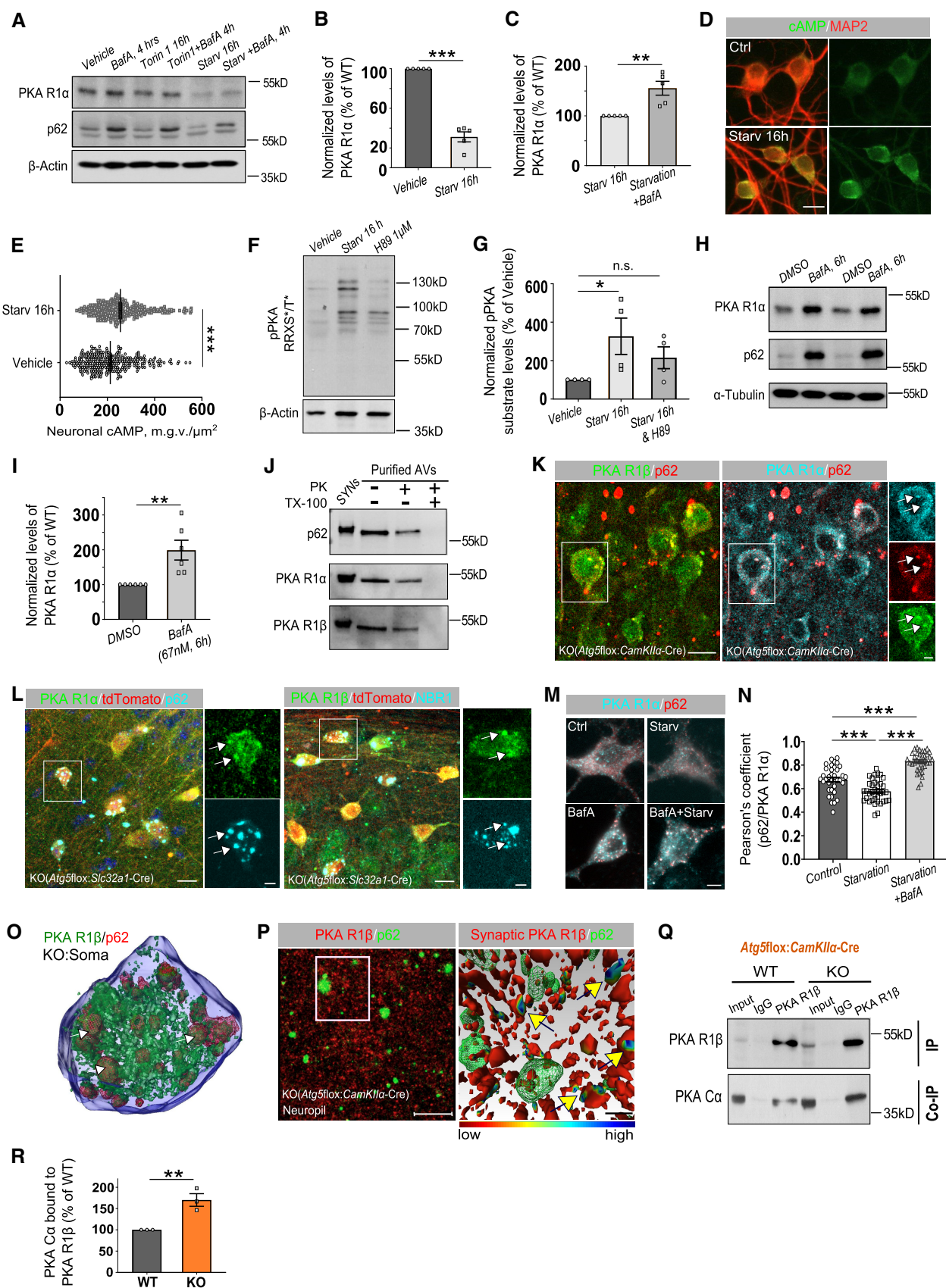
Figure 4.

◀

Figure 4. PKA R1α/β subunits of the PKA complex are degraded by autophagy in neurons.

A   Western Blot analysis of PKA R1α protein levels in NSC34 cells, treated with 250 nM Torin1 or deprived of amino-acids and serum for 16 h. Lysosomal degradation was blocked in the last 4 h using 67 nM of Bafilomycin A (BafA).

B   Starvation significantly reduced PKA R1α protein levels in NSC34 cells (vehicle set to 100%, starvation: $31.19 \pm 5.085\%$, $P < 0.0001$, one-tailed unpaired t-test). $n = 5$.

C   Application of 67 nM BafA for 4 h before harvesting was sufficient to stabilize the PKA R1α protein levels in starved NSC34 cells (starvation set to 100%, starvation + BafA: $155.5 \pm 13.93\%$, $P = 0.002$, one-tailed unpaired t-test). $n = 5$.

D, E   16 h starvation significantly increased intracellular cAMP level measured as mean intensity in MAP2-positive cultured primary neurons (Vehicle: 212.4 ± 5.619, Starvation: 255.1 ± 5.715; $P < 0.0001$, two-tailed paired t-test). $n_{Vehicle} = 314$, $n_{starvation} = 306$ neurons from $n = 3$.

F, G   Phosphorylation state of proteins containing PKA substrate RRXS/T motif was increased upon 16 h of amino-acid and serum starvation in primary cortico-hippocampal neurons at DIV14 and was suppressed by 1 μM H89 supplementation in the media (Vehicle set to 100%, Starvation: $326.60 \pm 94.53\%$, H89: $214.80 \pm 56.87\%$, $P = 0.033$, one-way ANOVA with Dunn's multiple comparison test). $n = 4$. The pPKA substrate levels were normalized to the total protein amount stained with Ponceau S.

H, I   Treatment of NSC34 cells with BafA (67 nM) for 6 h significantly increased PKA R1α protein levels compared to the DMSO-treated group set to 100% (BafA: $198.9 \pm 28.44\%$, $P = 0.003$, one-tailed unpaired t-test). $n = 6$.

J   Western blot analysis of purified autophagosomes (AVs) (50 μg AVs/lane) with and without Proteinase K (PK) treatment. TX-100 (1% final) was used as a positive control for the activity of PK. Synaptosome lysates (Syn, 30 μg/lane) were used as a positive control for the signal of antibodies.

K, L   Representative confocal images of the hippocampus CA1 area from *Atg5*flox:*CamKIIα*-Cre (K) and *Atg5*flox:*Slc32a1*-Cre (L) KO mice, immunostained for PKA R1-α/β and co-immunostained for p62 and/or NBR1. White rectangular boxes indicate areas magnified to the right. White arrows indicate p62/NBR1 inclusion bodies positive for PKA R1. Scale bar: large panel 15 μm, small panel: 5 μm. Representative pictures for WT controls are shown in Appendix Fig S6D–F.

M, N   Representative fluorescent images and subsequent analysis of PKA R1- α/p62 colocalization (Pearson's correlation coefficient) in primary cortico-hippocampal neurons, which have undergone 16 h amino-acids and serum starvation and were additionally treated with BafA (67 nM) to visualize the lysosomes (control: 0.68 ± 0.019, starvation: 0.58 ± 0.015, starvation + BafA: 0.83 ± 0.014; $P_{control\ vs\ starvation} < 0.0001$, $P_{control\ vs\ starvation+BafA} < 0.0001$, $P_{starvation\ vs\ starvation+BafA} < 0.0001$ Ordinary one-way ANOVA with Tukey's multiple comparison test). $n_{control} = 36$, $n_{starvation} = 38$, $n_{starvation+BafA} = 36$ neurons from $n = 3$. Scale bar: 5 μm.

O, P   3D-reconstruction of *Atg5*flox:*CamKIIα*-Cre KO soma (O), as well as the immunohistochemical profile and the 3D surface rendering of *Atg5*flox:*CamKIIα*-Cre KO neuropil (P) revealing the PKA R1-β/p62 colocalization in the soma (white arrows), but not in processes (yellow arrows). Scale bar: 10 μM.

Q, R   Co-immunoprecipitation of endogenous PKA R1-β with PKA-Cα from *Atg5*flox:*CamKIIα*-Cre WT/KO mouse brain lysates (WT set to 100%, KO: $170.3 \pm 14.88\%$, $P = 0.005$, one-tailed unpaired t-test, $n = 3$). Input, 1.5% of the total lysate was added to the assay.

Data information: *$P < 0.05$; **$P < 0.01$; ***$P < 0.001$. All data represent mean $\pm$ SEM. All n represent biological replicates.
Source data are available online for this figure.

5 min, whereas this effect was diminished upon ATG5 deficiency (Fig 5A and B). To investigate whether neuronal ATG5 regulates PKA/pCREB activation *in-vivo*, we analyzed forskolin-dependent pCREB responses in cortical neurons isolated from 8-week-old *Atg5*flox:*CamKIIα*-Cre:*Ai9* WT or KO mice using quantitative high content screening microscopy. Our analysis revealed that forskolin-mediated activation of pCREB was abolished in cortical excitatory KO neurons in adult mice (Fig 5C and D). These changes were independent of the cAMP level *per se*, which was unaltered in both hippocampal brain lysates (Appendix Fig S7A) and isolated cortical neurons of *Atg5*flox:*CamKIIα*-Cre:*Ai9* KO mice (Appendix Fig S7B and C). Activation of pCREB using a brief pulse of depolarizing KCl solution (40 mM) was also impaired (Fig 5D), suggesting that ATG5 could regulate neuronal activity-dependent pCREB activation.

CREB belongs to the CREB1/CREM transcription factors subgroups, which bind to cAMP-responsive elements in target genes. To understand whether alterations of PKA signaling are reflected in the expression of CREM1/CREB target genes, we analyzed the gene expression in FACS-sorted *Atg5*flox:*Slc32a1*-Cre:*Ai9* WT and KO neurons using the next-generation sequencing approach (Fig 5E). We identified that ATG5 deletion caused downregulation of 732 transcripts (Dataset EV2). Although only eight genes were differentially expressed based on their corrected P-value (FDR < 0.05, Appendix Fig S7D), analysis of transcription factor binding signatures ($P < 0.01$, FC < −2, 115 genes in total) revealed that 29.6% of downregulated genes contained CREB1 response elements in their promoter region (Fig 5F). On the other hand, 66 out of 238 significantly upregulated genes ($P < 0.01$, FC > 2) were regulated by the transcription activity WT1 (Fig 5G), which has recently been

described as a crucial regulator of synaptic function and neuronal excitability (Mariottini *et al*, 2019). Intriguingly, among downregulated genes with CREB1 response elements, we identified genes encoding for proteins with a function in protein and vesicle trafficking (*Clasp1*, *Gdi2*, *Sgms1*, *Vps13b*; Fig 5H), suggesting that autophagy might indirectly regulate intracellular membrane trafficking by controlling the PKA/CREB1 signaling.

If neuronal levels of PKA R1 subunits are negatively regulated by starvation (see Fig 4), starvation should facilitate CREB translocation to the nucleus due to its increased phosphorylation by liberated PKA catalytic subunit. In agreement with this hypothesis, a proportion of neurons with nuclear pCREB was significantly increased upon amino acid and serum deprivation (Fig 5I). This phenotype was PKA-dependent since blocking the catalytic activity of PKA by the ATP-site inhibitor H89 diminished pCREB translocation to the nucleus (Fig 5J).

Neuronal ATG5 regulates PKA-mediated phosphorylation of proteins enriched at the PSD of excitatory synapses

In addition to its crucial function in regulating CREB-dependent gene expression, PKA can directly phosphorylate synaptic proteins (Greengard *et al*, 1991; Cho *et al*, 2015). Our results above raise the question of whether autophagy can directly regulate PKA-dependent phosphorylation of the synaptic proteome. When PKA is activated, it phosphorylates substrates preferably on the recognition motif Arg-Arg-X-Ser/Thr-Y, and phosphorylated phospho-Ser/Thr residues can be monitored by using a specific antibody (RRXS/T). In WT neurons, application of forskolin induced an
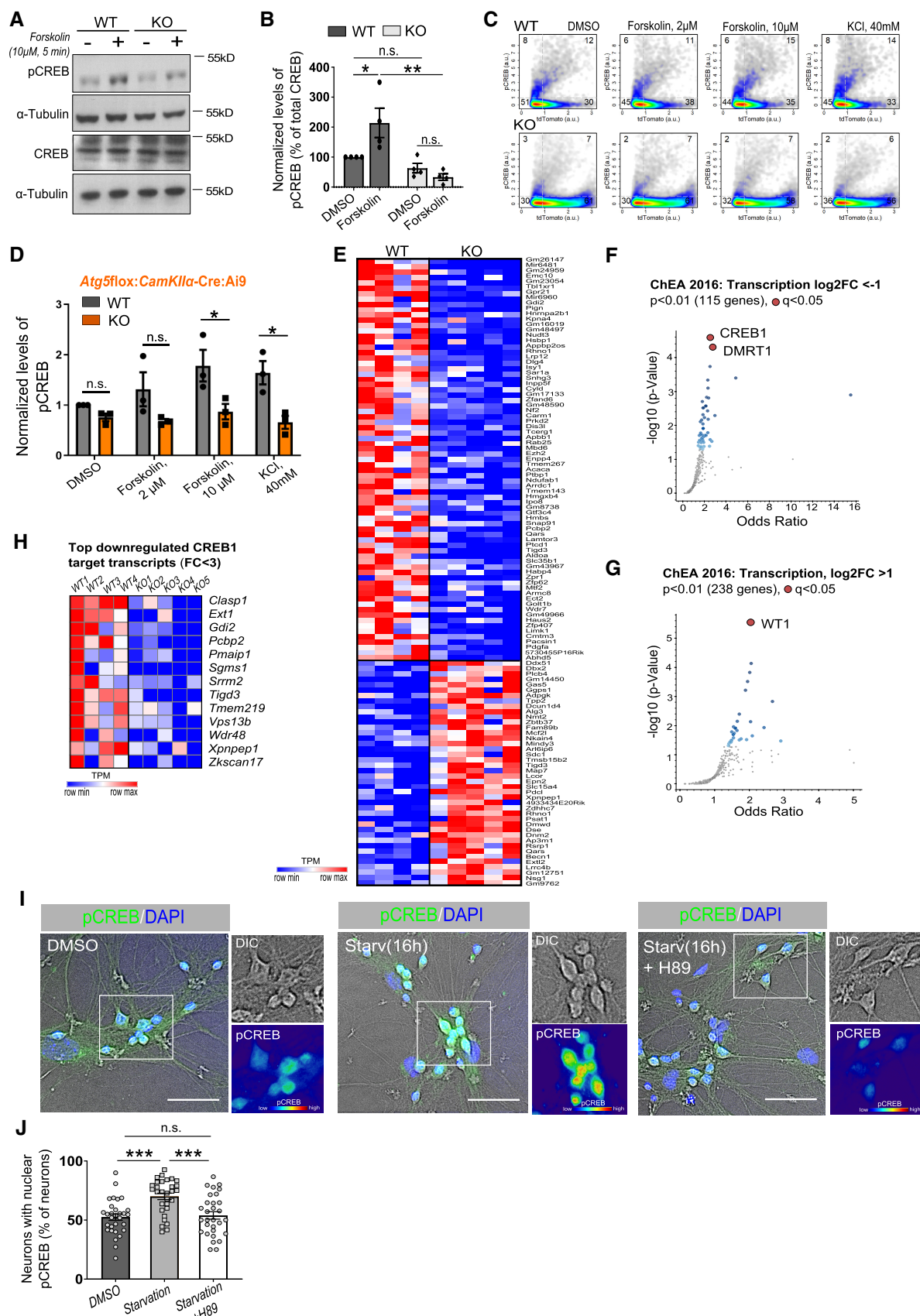
Figure 5.

Figure 5. ATG5 regulates neuronal cAMP/PKA/pCREB signaling.

A, B   Western Blot analysis of pCREB protein levels in *Atg5*flox:*CAG*-Cre[Tmx] WT/ KO cultured neurons at DIV14, treated with forskolin (WT$_{DMSO}$ set to 100%, WT$_{Forskolin}$: 214.17 ± 48.87%, KO$_{DMSO}$: 63.26 ± 15.85%, KO$_{Forskolin}$: 33.50 ± 10.84%, $P_{WT\ DMSO/WT\ Forskolin}$ = 0.042, $P_{WT\ Forskolin/KO\ Forskolin}$ = 0.002, two-way ANOVA with Tukey's multiple comparisons). n = 4. The same lysates were run in parallel to detect pCREB and CREB and normalized to their respective loading control before calculating the pCREB/CREB ratio.

C, D   High-content screening microscopy analysis of pCREB fluorescence intensity in neurons isolated from 8 to 12-week-old *Atg5*flox:*CamKIIα*-Cre:*Ai9* WT/KO mice, treated either with DMSO or with 2 μM, 10 μM Forskolin or 40 mM KCl (WT$_{DMSO}$ set to 1, KO$_{DMSO}$: 0.76 ± 0.07, WT$_{Forskolin\ 2\ μM}$: 1.31 ± 0.34, KO$_{Forskolin\ 2\ μM}$: 0.68 ± 0.04, WT$_{Forskolin\ 10\ μM}$: 1.78 ± 0.31, KO$_{Forskolin\ 10\ μM}$: 0.87 ± 0.15, WT$_{KCl\ 40\ mM}$: 1.64 ± 0.23, KO$_{KCl\ 40\ mM}$: 0.66 ± 0.13, $P_{WT\ Forskolin\ 10\ μM/KO\ Forskolin\ 10\ μM}$ = 0.047, $P_{WT\ KCl\ 40\ mM/KO\ KCl\ 40\ mM}$ = 0.034, two-way ANOVA with Tukey's multiple comparisons test). n = 3.

E   Next-generation RNA sequencing-based Kallisto transcriptome output of FACS-sorted neurons isolated from 3-week-old *Atg5*flox:*Slc32a1*-Cre:*Ai9* WT/KO mice (cut-off P < 0.02, FC < −2/> 2; n_{WT} = 4, n_{KO} = 5). See also Dataset EV2 and Appendix Fig S7D for differential gene expression analysis.

F, G   EnrichR-based analysis of transcription factor-binding site enrichment using ChEA2016 databank. Analysis was applied to differentially downregulated (F) and upregulated (G) gene sets (cut off P < 0.01, log2FC < −1/> 1), obtained using Sleuth-based algorithm for gene expression analysis of RNA transcriptome shown in (E).

H   Top downregulated CREB1 target genes in autophagy-deficient FACS-sorted *Atg5*flox:*Slc32a1*-Cre:*Ai9* KO neurons.

I, J   Representative fluorescent images and subsequent analysis of primary cortico-hippocampal neurons containing nuclear pCREB either under DMSO-treated condition or under condition when amino acids and serum starvation was induced for 16 h in the absence or presence of 1 μM of PKA inhibitor H89. Neurons were identified by their polarized morphology in DIC. White rectangular boxes indicate panel magnified to the right. In the inserts, LUT gradient was added to highlight the pCREB intensity in the nucleus. Scale bar: 50 μm. DMSO: 52.50 ± 2.757, starvation: 70.00 ± 2.697, starvation + H89: 53.92 ± 3.147; $P_{DMSO/starvation}$ < 0.0001, $P_{starvation/starvation\&H89}$ = 0.0004, one-way ANOVA with Tukey's multiple comparisons test, n = 30 images from n = 3 independent experiments.

Data information: *P < 0.05; **P < 0.01; ***P < 0.001. All data represent mean ± SEM. All n represent biological replicates.

Source data are available online for this figure.

---

increase in phosphorylated phospho-Ser/Thr residues (Fig 6A), whereas forskolin-dependent phosphorylation of PKA substrates was decreased in neurons lacking ATG5 *in-vitro* (Fig 6B) and *in-vivo* (Appendix Fig S7E and F), suggesting a global reduction in PKA-dependent phosphoproteome upon autophagy deficiency. To further define specific phosphorylation targets affected by neuronal ATG5 deletion, we investigated the phosphoproteome of *Atg5*flox:*CamKIIα*-Cre and *Atg5*flox:*Slc32a1-Cre* WT and KO brains using the spike-in SILAC mouse approach described above (see Appendix Fig S3A). This analysis yielded the identification of in total 104 significantly up- or downregulated (P < 0.05, FC > 1.2/ < −1.2) phosphosites in *Atg5*flox:*CamKIIα*-Cre and 217 phosphosites in *Atg5*flox:*Slc32a1-Cre* lines whose abundance, when normalized to total protein levels, changed upon ATG5 KO condition. Of them, 31 and 82 phosphosites were decreased in *Atg5*flox: *CamKIIα*-Cre KO and *Atg5*flox:*Slc32a1-Cre* KO mice, respectively (FC < −1.2, P < 0.05, Dataset EV3). Interestingly, in both mouse lines, gene products in which neuronal ATG5 deletion decreased phosphorylation included several scaffolding postsynaptic and a few presynaptic proteins (PALM, TNIK, DNAJC5, DLGAP4, RIMS1, EPB4.1L1, DLG1, SYNGAP1, and CASKIN1; Fig 6C) and were clustered in GO cellular component terms related to postsynaptic density (PSD) of glutamatergic synapses (Fig 6D). These data argue that a lack of autophagy reduces global phosphorylation of PSD proteins at glutamatergic synapses.

Phosphorylation of PKA substrates in neurons is maintained at a relatively high state under basal conditions (Hilfiker *et al*, 2001). Therefore, the global phosphorylation changes in brains lacking ATG5 may be due, at least in part, to decreased PKA signaling. To directly test this hypothesis, we first performed an analysis of PKA phosphorylation substrates in forskolin-stimulated cortical slices of *Atg5*flox:*CamKIIα*-Cre WT mice (Fig 6E; Dataset EV4). Forskolin caused an increase in phosphorylation of several known PKA substrates, such as MAPT, RIMS1, STMN1, IP3R1, SNAP-25 most of which were enriched at the PSD of excitatory synapses (Appendix Fig S8A). By comparing PKA-dependent substrates in WT (FC < −1.2, P > 0.05) and phosphorylation targets identified in

total phosphoproteome of autophagy-deficient brains (see Fig 6C), we found that 11 substrates from *Atg5*flox:*CamKIIα*-Cre KO brains and 25 substrates from *Atg5*flox:*Slc32a1-Cre* KO mice could be potential PKA targets (Appendix Fig S8B). Subsequent analysis of these 36 substrates revealed that 20 of them contained a potential PKA phosphorylation motif and were less sensitive to forskolin treatment in *Atg5*flox:*CamKIIα*-Cre KO cortical slices (Fig 6F; Appendix Fig S8C and D). PKA substrates, identified by co-immunoprecipitation in cortical WT lysates with PKA phosphorylation state-specific antibody (RRXS/T) were also enriched at the PSD as such (Appendix Fig S8E and F), whereas comparison of these targets with proteins identified in global phosphoproteome analysis of conditional ATG5 KO mice again yielded candidates confined to the PSD of excitatory synapses (Appendix Fig S8G and H). Finally, we found that the vast majority of substrates significantly downregulated in global KO phosphoproteome (see Fig 6C) were not reacting to forskolin treatment in acute cortical slices prepared from *Atg5*flox:*CamKIIα*-Cre KO mice (Fig 6G) and those forskolin- "irresponsive" targets were enriched at the PSD of glutamatergic synapses (Fig 6H; Dataset EV4). Interestingly, PKA signaling was not completely abolished upon forskolin stimulation of *Atg5*flox: *CamKIIα*-Cre acute KO slices (Appendix Fig S8C; see also Fig 6A), likely as a result of the release of the sequestered catalytic subunit by elevated cAMP levels.

The data described so far suggest that ATG5 indirectly regulates synaptic function by controlling PKA-dependent phosphorylation of PSD-confined proteins. To directly test this hypothesis, we employed a FRET-FLIM-based reporter of PKA activity targeted to PSD-95, AKARet-PSD (Tang & Yasuda, 2017). Application of forskolin and IBMX (an inhibitor of cAMP-degrading phosphodiesterase) to AKARet-PSD-expressing WT primary cortical neurons induced a decrease in fluorescence lifetime (increase in FRET) in spines with the time course of 4–6 min (Fig 6I). This effect was abolished in neurons lacking ATG5 (Fig 6J), indicating that ATG5 regulates PKA-dependent phosphorylation of proteins in the dendritic spine. The posttranslational modification of PSD proteins by serine/threonine phosphorylations has been shown to have a
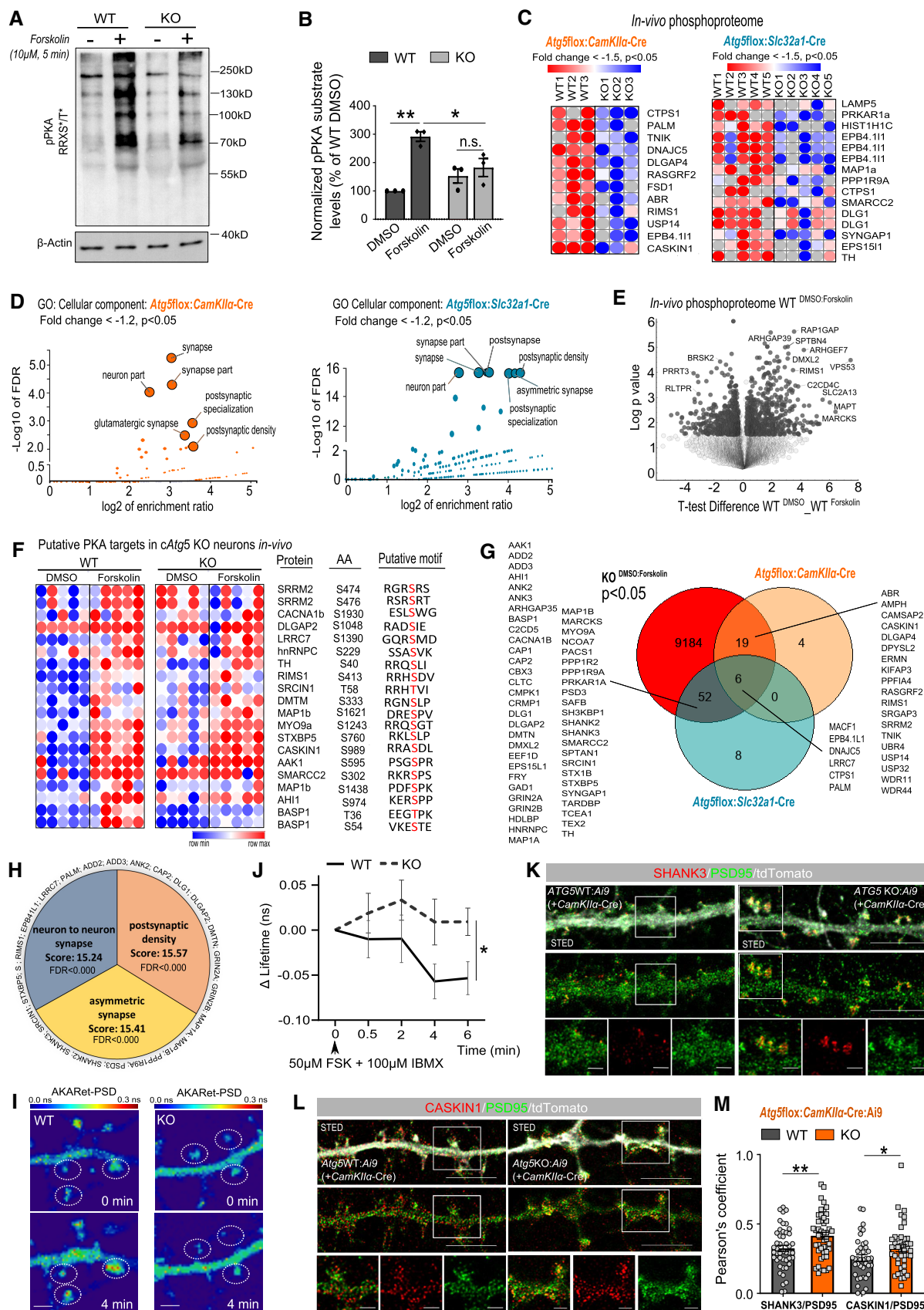
Figure 6.

Figure 6. ATG5 regulates PKA-mediated phosphorylation of proteins enriched at the PSD of excitatory synapses.

A, B   Western Blot analysis of PKA substrates carrying RRXS/T motif in primary cortico-hippocampal $Atg5$flox:CAG-Cre^{Tmx} WT/KO neurons at DIV14, treated with Forskolin (WT$_{DMSO}$ set to 100%, WT$_{Forskolin}$: 291.85 ± 17.02%, KO$_{DMSO}$: 152.97 ± 25.26%, KO$_{Forskolin}$: 182.56 ± 31.89%, $P_{WTDMSO/WTForskolin}$: 0.001, $P_{WTForskolin/KOForskolin}$: 0.033, two-way ANOVA with Tukey's multiple comparisons). $n = 3$.

C   The top downregulated phosphopeptides (cut-off $P < 0.05$, Fold change < -1.5) in either cortical lysates of $Atg5$flox:$CamKII\alpha$-Cre KO ($n = 3$) or striatal lysates of $Atg5$flox:$Slc32a1$-Cre KO mice ($n = 5$), identified by global phosphoproteome analysis. The levels of phosphopeptides were normalized to their total protein levels. See also Dataset EV3.

D   WebGestalt- based GO analysis of "cellular component"-enriched terms among significantly downregulated phosphopeptides (cut-off $P < 0.05$, Fold change < -1.2) in $Atg5$flox:$CamKII\alpha$-Cre KO (left) and $Atg5$flox:$Slc32a1$-Cre KO (right) brains.

E   Volcano plot of phosphopeptides identified using label-free phosphoproteome analysis of acute cortico-hippocampal slices from $Atg5$flox:$CamKII\alpha$-Cre WT mice treated either with DMSO or 50 μM Forskolin for 15 min ($n = 5$). Phosphopeptides significantly upregulated ($P < 0.05$) upon Forskolin treatment are highlighted in dark gray.

F   Heat map representation of LFQ intensities of common phosphopeptides, identified in (E) and containing putative PKA phosphorylation motif (predicted by Perseus software) in $Atg5$flox:$CamKII\alpha$-Cre WT and KO acute slices, treated either with DMSO or 50 μM Forskolin for 15 min ($n = 5$).

G   Venn diagram showing the number of phosphopeptides significantly downregulated in $Atg5$flox:$CamKII\alpha$-Cre KO and $Atg5$flox:$Slc32a1$-Cre KO brains (cut-off $P < 0.05$, Fold-change < -1.2) and the phosphophopeptides, which were "irresponsive" to Forskolin treatment in $Atg5$flox:$CamKII\alpha$-Cre KO acute slices ($P > 0.05$).

H   Top three enriched "cellular component" terms obtained by GO analysis of common phosphopeptides identified in (G).

I   Fluorescence lifetime images of AKARet-PSD at spines of ATG5 WT and KO cortico-hippocampal neurons before and 4 min after Forskolin and IBMX administration. Scale bar: 1 μm. Drawn contours represent single spines of WT or KO neurons.

J   Averaged timecourses of fluorescence lifetime change of AKAR-PSD in WT and ATG5 KO spines (WT$_{6 min}$: −0.053 ± 0.018, KO$_{6 min}$: 0.009 ± 0.015; $P = 0.026$, two-tailed unpaired t-test. n_{WT}: 50/5, n_{KO}: 58/6 (spines/neurons) from $n = 3$ independent experiments.

K–M   Representative STED images and Pearson's colocalization coefficient analysis of SHANK3 (K) and CASKIN1 (L) and PSD95 in $Atg5$flox:$CamKII\alpha$-Cre:$Ai9$ WT/KO neurons. Scale bar: 5 μm, 1 μm (small panels). WT$_{SHANK3}$: 0.324 ± 0.022, KO$_{SHANK3}$: 0.415 ± 0.024; $P = 0.0067$, two-tailed unpaired t-test. n_{WT} = 46, n_{KO} = 46. WT$_{CASKIN1}$: 0.255 ± 0.024, KO$_{CASKIN1}$: 0.326 ± 0.025; $P = 0.0432$, two-tailed unpaired t-test. n_{WT} = 39, n_{KO} = 43 from $n = 2$ independent experiments.

Data information: *$P < 0.05$; **$P < 0.01$; ***$P < 0.001$. All data represent mean ± SEM. All n represent biological replicates.
Source data are available online for this figure.

profound effect on the dynamics of their localization. For instance, the anchoring of DLG at synapses is optimal when DLG is in the dephosphorylated state (Koh *et al*, 1999). If ATG5-dependent cAMP/PKA signaling is a crucial regulator of phosphorylation of PSD-confined proteins, then decreased phosphorylation of these proteins in the absence of ATG5 could alter their localization. Consistent with this hypothesis, colocalization of SHANK3 and/or CASKIN1 and PSD95 was significantly increased in ATG5 KO neurons analyzed by superresolution STED microscopy compared with WT neurons (Fig 6K–M). This phenotype was also associated with an increased density of PSD in neurons lacking ATG5, whereas the SV pool remained unchanged (Appendix Fig S8I–K).

Autophagy-dependent PKA signaling regulates AMPARs localization and function

What are the implications of decreased phosphorylation of PSD proteins for the physiology of ATG5 KO neurons? The PSD of synapses includes cytoskeletal scaffold proteins, receptors and ion channels, and it is known that the phosphorylation state of these components is central to synaptic transmission (Esteban *et al*, 2003). The size of PSD is a common feature of neuronal excitability *per se*, with larger PSD size positively correlating with higher numbers of AMPA-type glutamate receptors (AMPARs) (Takumi *et al*, 1999; Tao-Cheng, 2019). Furthermore, PKA directly regulates synaptic function via activity-dependent internalization of AMPAR subunit GLUR1 from the postsynaptic plasma membrane (Lee *et al*, 2003). This function of PKA requires the interaction of its R2α-subunit with AKAP79/150 (Tavalin *et al*, 2002) and involves the phosphorylation of GLUR1 at Ser845 (Esteban *et al*, 2003). Levels of AKAP79/150 (also known as AKAP5) and GLUR1 phosphorylated at Ser845 were unaltered in hippocampal lysates from $Atg5$flox:$CamKII\alpha$-Cre KO mice, whereas a slight but nonsignificant reduction in GLUR1

phosphorylation and a decrease in total levels of AKAP79/150 were detected in the hippocampus of $Atg5$flox:$Slc32a1$-Cre KO mice (Appendix Fig S9A–F).

Because the absence of changes in PKA-dependent GLUR1 phosphorylation in excitatory neurons does not explain the changes in excitability in $Atg5$flox:$CamKII\alpha$-Cre KO mice (see Fig 1), we took a closer look at the molecular function of proteins with decreased phosphorylation in mice lacking neuronal ATG5. In agreement with the fact that PKA phosphorylates multiple cytoskeletal substrates in non-neuronal cells (Shabb, 2001), "cytoskeletal protein binding" (32% of proteins) and "actin-binding" (20% of proteins) were the most abundant GO molecular function terms among downregulated phospho-targets in autophagy-deficient neurons (Fig 7A; Dataset EV4). Strikingly, analysis performed using the human phenotype ontology database indicated that proteins identified as being decreased in their phosphorylation state in brains from mice with autophagy deficits are associated with EEG abnormality and seizure onset in humans (Fig 7A). These data, taken together with the fact that about 37% of "cytoskeletal protein binding" proteins identified in Fig 6G are directly involved in endocytosis and trafficking of GLUR1 subunit of AMPARs (CLTC, ANK3, DLG1, DPYSL2, EPB41L1, PPP1R9A, SHANK3 and STXBP5; Leonard *et al*, 1998; Carroll *et al*, 1999; Shen *et al*, 2000, 2020b; Uchino *et al*, 2006; Wu *et al*, 2008; Smith *et al*, 2014; Zhang *et al*, 2020; Fig 7B), prompted us to speculate that altered GLUR1 trafficking, rather than its direct phosphorylation by PKA is a crucial determinant of neuronal excitability in ATG5 KO neurons. In line with this hypothesis and the data described above (see Fig 6K–M), the colocalization of GLUR1 and postsynaptic density marker PSD95 was increased in cultured neurons lacking ATG5 (Appendix Fig S9G and H). To test the effect of acute ATG5 deletion on the synaptic localization of GLUR1, we analyzed GLUR1 levels in spines of excitatory neurons of 12–13-week-old $Atg5$wt/wt:$Ai9$ and $Atg5$flox/flox:$Ai9$ mice that

had received a stereotactic injection of *CamKIIα*-Cre adeno-associated virus (AAV) into the CA1 area of the hippocampus (Fig 7C). We found that GLUR1 levels were significantly increased in ATG5-deficient dendritic spines compared with controls (Fig 7D). In addition, the loss of ATG5 also altered the ratio of GLUR1 on spines to shaft, resulting in an accumulation of more GLUR1 at spines compared with shafts (Fig 7E and F). This phenotype results directly from loss-of-function of ATG5, as overexpression of ATG5 tagged with eGFP (the construct shown to be functional in overexpression studies in Negrete-Hurtado *et al*, 2020) decreases PSD-confined GLUR1 localization (Fig 7G and H). On the other hand, overexpression of PKA R1α/β in control neurons mimicked the phenotype of ATG5 KO and caused the accumulation of GLUR1 at the PSD (Fig 7I and J). To directly probe whether the defects in GLUR1 distribution reflect the accumulation of GLUR1 on the plasma membrane, we employed GLUR1-pHluorin, a fusion between the N-terminus of GLUR1 and a pH-sensitive variant of GFP that undergoes quenching within the acidic vesicle lumen and is dequenched upon exocytic fusion with the plasma membrane. In ATG5 KO neurons, superfused with buffers titrated either to pH 5.5 (to reveal the surface exposure of pHluorin) or to pH 8.5 (to reveal the total levels of pHluorin; Appendix Fig S9I), we observed a significant elevation of the surface-stranded/total GLUR1-pHluorin ratio compared to WT neurons (Appendix Fig S9J and K).

In contrast to the majority of AMPARs, which contain GLUR2, GLUR1-containing AMPARs are Ca^{2+} permeable (Jonas & Burnashev, 1995). Thus, we next wondered whether the increased density of GLUR1-containing AMPARs was the cause of the neuronal hyperexcitability observed in *Atg5*flox:*CamKIIα*-Cre KO mice (see Fig 1) due to the increased Ca^{2+} influx upon neuronal activity. We first employed the genetically encoded Ca^{2+}—sensing probe GCAMP7f to monitor Ca^{2+} signals in primary cortico-hippocamapal neurons isolated from *Atg5*wt:wt/*Ai9* or *Atg5*flox:flox/*Ai9* mice and transduced with an AAV encoding a *CamKIIα*-GCaMP7f construct and, additionally, with *CamKIIα*-Cre AAV to induce a KO. As the GCaMP7f reporter is controlled by a *CamKIIα* promoter, only neuronal Ca^{2+} signals from excitatory neurons were captured. We analyzed the Ca^{2+} responses evoked by tetanic stimulation (four tetani, 100 APs at 100 Hz, 3 s interval) in the cell soma (Fig 7K–M) and dendrites (Appendix Fig S9L) and found that KO excitatory neurons had significantly increased facilitation of evoked calcium signals compared to controls. This facilitation was completely abolished by pre-incubation of KO neurons with the broad-spectrum AMPA/kainate receptor antagonist CNQX, confirming that neuronal excitability in autophagy-deficient neurons is driven by glutamate-bound AMPARs (Fig 7M). Notably, the application of CNQX for 5 min also reduced the facilitation in WT, albeit with less efficiency, indicated by a significant difference between the two groups, but not in multiple comparison analysis (Appendix Fig S9M). More importantly, the differences in evoked dendritic Ca^{2+} signals between genotypes were abolished when external calcium Ca^{2+} was changed from 2 to 0 mM (Appendix Fig S9N and O), indicating that the observed changes in dendritic Ca^{2+} signals in ATG5 KO neurons are not due to the release of Ca^{2+} from internal stores (e.g. ER). This function of autophagy in regulating neuronal excitability required PKA activity, as the application of the PKA inhibitor H89 reproduced the facilitation of evoked Ca^{2+} responses in control neurons (Fig 7N and O). Moreover, long-term application of the cAMP booster forskolin (72 h)

was sufficient to reduce the frequency of action potential firing in excitatory ATG5-KO primary neurons measured by microelectrode array (MEA) technology, whereas the frequency of action potentials in WT neurons was not altered (Fig 7P–R).

Finally, to determine whether ATG5 KO-induced changes in synaptic GLUR1 levels lead to altered properties of AMPAR currents, we performed whole-cell patch-clamp recordings of cortical pyramidal neurons. We recorded spontaneous AMPAR-mediated excitatory postsynaptic currents (sEPSCs) in acute brain slices of 12–13-week-old *Atg5*flox:flox mice, which received a stereotactic injection of either control AAV (*CamKIIα*-eGFP) or *CamKIIα*-Cre-eGFP AAV into the layer II/III of the perirhinal cortex. We found that acute ATG5 deletion in these cortical excitatory neurons significantly increased both the amplitude and the frequency of AMPA-mediated sEPSCs (Fig 7S and T). Taken together, these data indicate that autophagy regulates synaptic physiology by controlling PKA-mediated phosphorylation of PSD proteins, a phenotype associated with functional changes in AMPAR-mediated synaptic currents.

Discussion

Autophagy is currently linked to neuronal function by mechanisms, which include its role in the clearance of damaged and/or defective intracellular components (Menzies *et al*, 2017). In this study, we find that autophagy does not primarily contribute to the regulation of bulk levels of SV and/or mitochondrial proteins in excitatory or inhibitory neurons in the mouse brain *in-vivo*. Instead, our data suggest that autophagy indirectly regulates synaptic function by controlling the PKA-dependent phosphorylation of postsynaptic scaffold proteins independently of their degradation. This function of autophagy requires the targeting of inhibitory PKA R1α and R1β subunits to neuronal autophagosomes and can be triggered by starvation, a treatment that elevates cAMP levels. cAMP causes dissociation of the PKA holoenzyme, releasing the PKA R1 subunits for autophagosomal degradation (Fig 8). We propose that starvation-induced PKA R1 degradation paired with function autophagy can amplify the cAMP action in neurons by allowing more catalytic subunits to escape PKA complex formation both during the acute cAMP stimulation and thereafter. A recent study reported enrichment of synaptic and mitochondrial fragment proteins in autophagosomes purified from a whole mouse brain (Goldsmith *et al*, 2022), whereas a significant accumulation of ER proteins was found in ATG5-deficient cultured cerebellar granular neurons (Kuijpers *et al*, 2021). Although we found several ER proteins in our FACS-based proteomic analysis of ATG5-deficient GABAergic striatal neurons (Fig 2B and D), our GO analysis did not identify the ER as a deregulated term (Fig 2E; Appendix Fig S3D–H). This may reflect the difference between the analysis of cultured neurons and neurons *in-vivo*, as well as the report of differential ERphagy requirements in neuronal subclasses in different brain regions. The lack of mitochondria fragment enrichment in our datasets is likely due to the mixed origin (neurons and glia) of autophagosomes profiled in the previous study (Goldsmith *et al*, 2022).

Several lines of evidence indicate that autophagy is a crucial regulator of PKA signaling at synapses. First, we demonstrate that ATG5-deficient neurons reveal an accumulation of synapse-confined PKA R1α/β, a phenotype that sequesters PKA catalytic subunit and

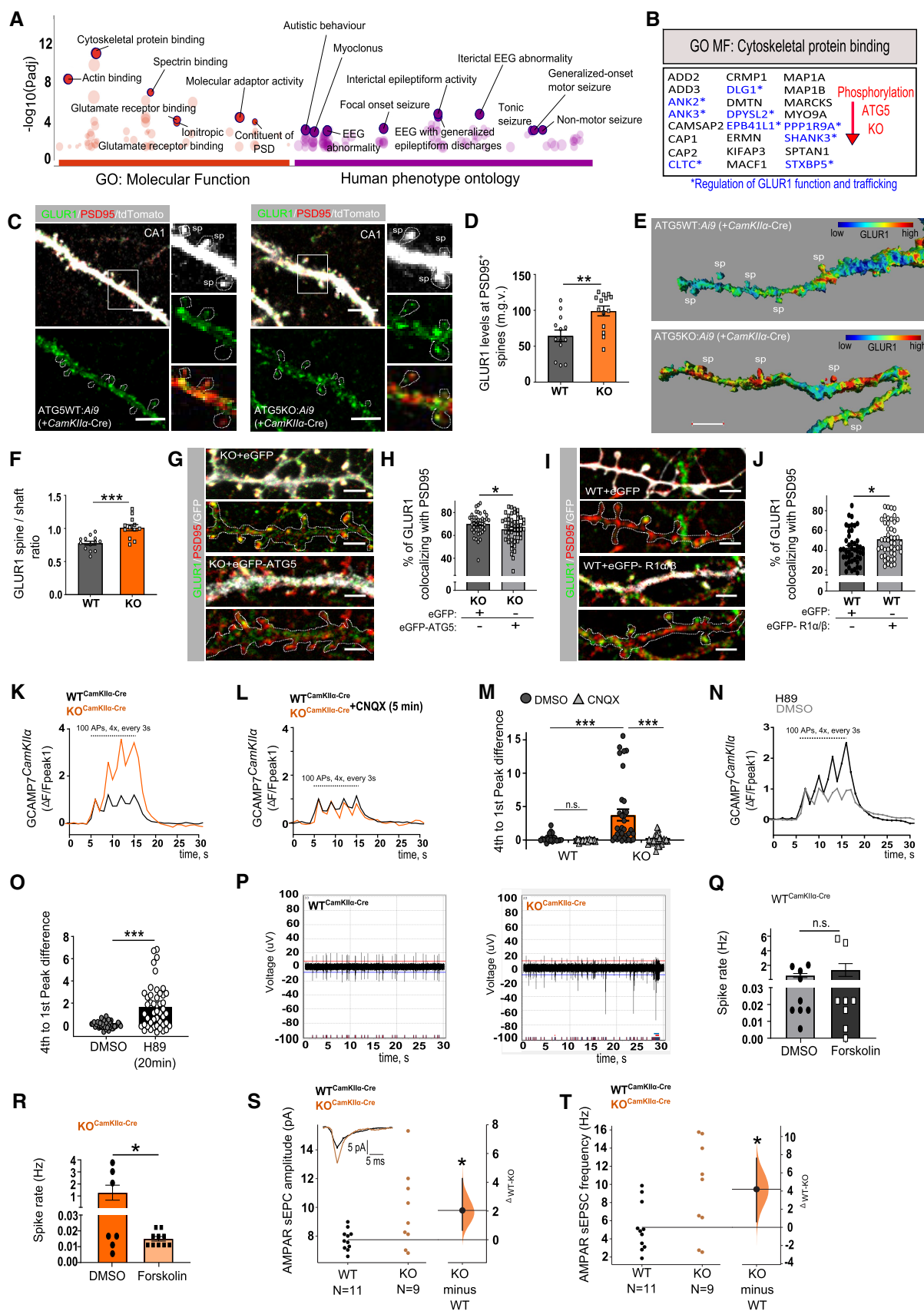Figure 7.

Figure 7. Autophagy-dependent PKA signaling regulates synaptic GLUR1 localization and AMPAR function.

A   g:Profiler-based analysis of GO molecular function and human phenotype enriched terms of "irresponsive" PKA target proteins in autophagy-deficient neurons identified in Fig 6G (cut-off $P < 0.05$, FC < -1.2). See also Dataset EV4.

B   Representation of proteins from GO molecular function term "cytoskeletal protein binding" shown in (A). Highlighted in blue are proteins with a published function in GLUR1 function and trafficking.

C, D   Analysis of GLUR1 fluorescent levels at the spines of 10–11 week-old *Atg5*wt/wt:*Ai9* and *Atg5*flox/flox:*Ai9* mice injected with *CamKIIα*-Cre AAV into the hippocampus. Scale bar: 5 µm. GLUR1 level at PSD95-positve spines were assessed measuring mean gray values after background subtraction (WT: 64.55 ± 7.988%, KO: 99.14 ± 6.863%; $P = 0.0029$, two-tailed unpaired *t*-test). $n_{WT} = 13$, $n_{KO} = 14$ images from $n = 3$ mice (> 31 dendritic spines analyzed per each mouse). sp, spine.

E   AMIRA-based color coded 3D-reconstruction of GLUR1 localization in dendrites of excitatory neurons of *Atg5*wt/wt:*Ai9* and *Atg5*flox/flox:*Ai9* mice injected with *CamKIIα*-Cre AAV into the hippocampus. sp, spine. Scale bar: 5 µm.

F   Analysis of GLUR1 concentration in the dendritic spines versus shaft. The mean gray value of GLUR1 at spines and shafts was measured separately and the spine value was divided by the shaft (WT: 0.778 ± 0.030, KO: 1.012 ± 0.046; $P = 0.0003$, n_{WT}: 13, n_{KO}: 12 images from $n = 3$ mice [> 31 dendritic spines/shaft analyzed per mouse]).

G   Representative fluorescence images of *Atg5*flox:*CAG*-Cre^Tmx WT/KO neurons transfected with eGFP or eGFP-ATG5 and immunostained for GLUR1, PSD95 and GFP. Scale bar: 5 µm.

H   The overexpression of eGFP-ATG5 in *Atg5*flox:*CAG*-Cre^Tmx KO neurons diminished the the GLUR1/PSD95 colocalization compared to the eGFP-overexpressing KO neurons (KO$_{eGFP}$: 70.07 ± 1.473%, KO$_{eGFP-ATG5}$: 65.42 ± 1.721%; $P = 0.048$, two-tailed unpaired *t*-test). $n_{KO + GFP} = 42$, $n_{KO + GFP-ATG5} = 50$ images from $n = 5$.

I, J   The coexpression of eGFP-PKA R1α and eGFP-PKA R1β in cultured *Atg5*flox:*CAG*-Cre^Tmx WT neurons results in significantly increased colocalization between GLUR1 and PSD95 compared to the eGFP-expressing neurons (WT: 42.30 ± 2.453%, KO: 51.32 ± 2.624%, $P = 0.014$, two-tailed unpaired *t*-test). $n_{WT + GFP} = 46$, $n_{WTGFP + PKA R1 OE} = 46$ images from $n = 3$. Analysis in (H, J) is performed using a unbiased custom-written Plugin for ImageJ.

K–M   GCAMP7f responses to tetanic stimulation (four tetani, 100 APs at 100 Hz, 3 s interval) in cell bodies of *CamKIIα*-Cre-transduced primary cortico-hippocampal *Atg5*wt:wt/*Ai9* (WT) and *Atg5*flox:flox/*Ai9* (KO) neurons expressing m*CamKIIα*-jGCaMP7f and treated either with DMSO (K) or with 10 µM CNQX for 5 min (L). Autophagy deficient cells showed significantly increased facilitation of GCAMP7f signal to electrical stimulation (ΔF/Fpeak1) compared to the WT, a phenotype which was blocked by the application of CNQX (WT$_{DMSO}$: 0.28 ± 0.12, WT$_{CNQX}$: −0.07 ± 0.03, KO$_{DMSO}$: 3.74 ± 0.86, KO$_{CNQX}$: −0.014 ± 0.13, $P_{WT DMSO/ KO DMSO} < 0.0001$, $P_{KO DMSO/KO CNQX} < 0.0001$, two-way ANOVA with Tukey's multiple comparisons test). $n_{WT DMSO} = 25$, $n_{WT CNQX} = 27$, $n_{KO DMSO} = 33$, $n_{KO CNQX} = 30$ neurons from $n = 3$. See also Appendix Fig S9L for changes in calcium signals in dendrites.

N, O   GCAMP7f responses to tetanic stimulation (four tetani, 100 APs at 100 Hz, 3 s interval) in primary cortico-hippocampal neurons expressing m*CamKIIα*-jGCaMP7f and treated either with DMSO or with 10 µM of H89 for 20 min (DMSO: 0.069 ± 0.042, H89: 1.668 ± 0.28, $P < 0.0001$, unpaired two-tailed *t*-test). $n_{DMSO} = 48$, $n_{H89} = 47$ neurons from $n = 3$ independent experiments.

P   Example traces of the network activity of primary cortico-hippocampal *CamKIIα*-eGFP AAV (WT)/ *CamKIIα*-Cre-eGFP AAV (KO)-transduced *Atg5*flox:flox neurons analyzed using the MEA system.

Q, R   Increased spike rate in ATG5 KO excitatory neurons is rescued by long-term application of Forskolin (10 µM for 72 h; WT$_{DMSO}$: 0.59 ± 0.29, WT$_{Forskolin}$: 1.35 ± 0.88, KO$_{DMSO}$: 1.27 ± 0.62, KO$_{Forskolin}$: 0.02 ± 0.001, $P_{KO DMSO/KO Forskolin} = 0.027$, unpaired two-tailed *t*-test). $n_{WT DMSO} = 9$, $n_{WT Forskolin} = 8$, $n_{KO DMSO} = 7$, $n_{KO Forskolin} = 10$ MEA chambers from three mice.

S, T   AMPAR-mediated sEPSCs in cortical pyramidal neurons of 12-week-old mice *Atg5*flox:flox mice, which were stereotactically injected either with *CamKIIα*-eGFP AAV (WT) or with *CamKIIα*-Cre-eGFP AAV (KO) into the perirhinal cortex layer II/III. (S) Amplitude of AMPAR sEPSC is increased in pyramidal KO neurons compared to the WT (WT: 7.75 ± 0.72 pA, KO: 9.79 ± 2.75 pA; $n_{WT} = 11$, $n_{KO} = 9$; unpaired mean difference between WT and KO (Δ$_{WT-KO}$): 2.04 [95%CI: 0.629, 4.22]; $P_{WT/KO} = 0.0152$ [two-sided permutation *t*-test]). Inset: representative traces of a WT sEPSC (petrol) and a KO sEPSC (ochre). (T) Frequency of AMPAR sEPSC is increased in pyramidal KO neurons compared to the WT (WT: 5.27 ± 2.66 Hz, KO: 9.47 ± 5.16 Hz; $n_{WT} = 11$, $n_{KO} = 9$, Δ$_{WT-KO}$: 4.19 [95%CI: 0.57, 7.56]; $P_{WT/KO} = 0.0326$ [two-sided permutation *t*-test]). Each data point represents the mean of a 1 min recording interval of an individual neuron. The filled curve indicates the resampled Δ distribution (5,000 bootstrap samples), given the observed data. Horizontally aligned with the mean of the test group, the Δ is indicated by the black circle. The 95% confidence interval of the mean difference is illustrated by the black vertical line.

Data information: *$P < 0.05$; **$P < 0.01$; ***$P < 0.001$. All data represent mean ± SEM. All n represent biological replicates.
Source data are available online for this figure.

impairs neuronal PKA signaling (Figs 3–5). Second, by analyzing the forskolin-induced phosphoproteome of acute brain slices, we demonstrate that ATG5 deletion decreases the phosphorylation state of several PKA targets confined to the PSD of glutamatergic synapses (Fig 6H). Finally, PKA signaling is reduced at the dendritic spines of ATG5 KO neurons (Fig 6I and J). Autophagy-dependent degradation of PKA R1α/β has an essential function in regulating synaptic levels of Ca^{2+} permeable GLUR1-containing AMPARs, and its loss leads to changes in functional properties of AMPAR-mediated synaptic currents (Fig 7). Although the augmented frequency of AMPAR-mediated sEPSCs described in the current study can also be a result of an increased number of synapses in autophagy-deficient neurons, our global proteome data analysis does not reveal changes in bulk levels of SV proteins. This data, taken together with our earlier findings, indicating no alteration in the number of spines in autophagy-deficient neurons (Negrete-Hurtado *et al*, 2020), suggests the upregulation in synaptic GLUR1 levels as a primary mechanism behind increased AMPA-mediated spontaneous neurotransmission. Previous work has shown that loss

of ATG5 in EMX1-derived progenitor cells increases excitatory presynaptic neurotransmission through a mechanism involving elevated calcium release from axonal ER stores (Kuijpers *et al*, 2021). Here, we describe that loss of ATG5 can also affect dendritic calcium signaling through a pathway dependent on extracellular calcium influx (Appendix Fig S9O) and AMPA receptors (Fig 7M).

One of the most intriguing findings of our study is that the autophagy-mediated PKA signaling primarily regulates the phosphorylation state of cytoskeletal scaffold proteins confined to the PSD of excitatory synapses, whereas its contribution to the regulation of presynaptic proteins is minor. Most candidates identified in our global phosphoproteomics analysis (including LRRC7, DLGAP4, SHANK3, STXBP5, SYNGAP1, EPB4.1L1) have recently been described as essential for PKA-dependent synaptic downscaling of glutamatergic neurons (Desch *et al*, 2021). Homeostatic synaptic scaling is achieved by up- or down-regulation of functionally available AMPARs at the PSD (Chowdhury & Hell, 2018). Our data suggest that neuronal autophagy may act as a potential modifier of homeostatic synaptic plasticity, although future studies are needed to support this hypothesis.
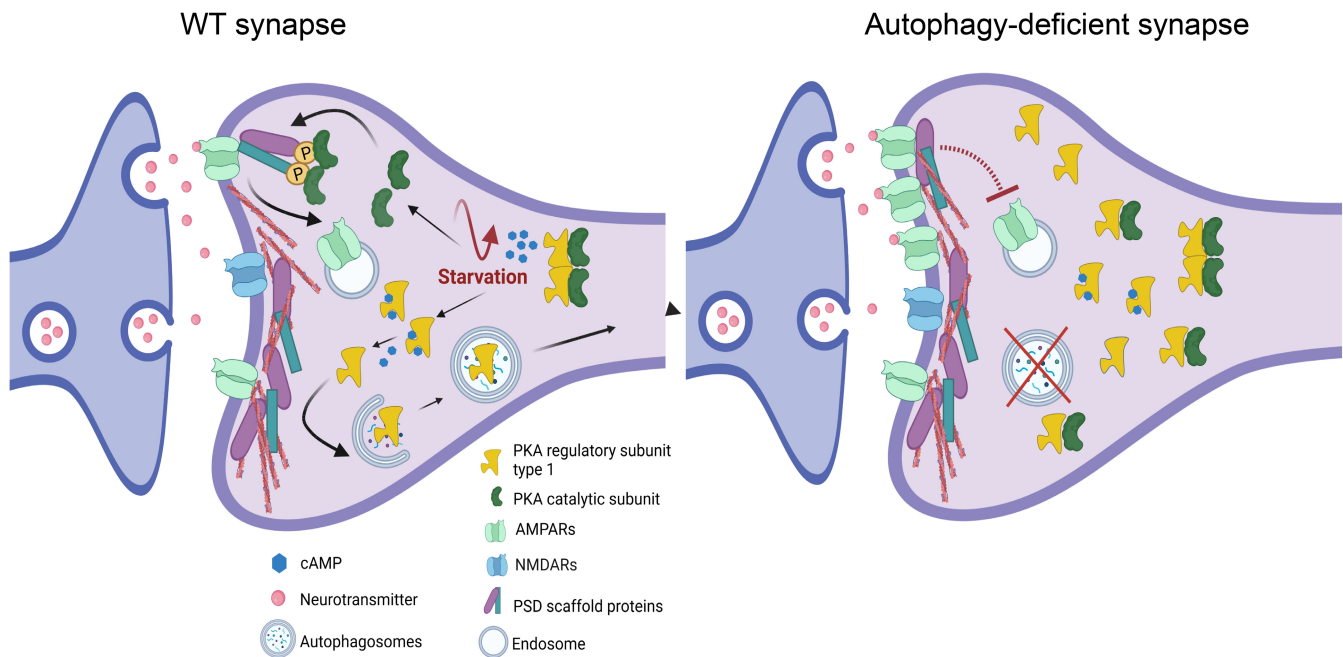
Figure 8. Hypothetic model of how autophagy regulates PKA signaling and AMPA receptor function at synapses.
Autophagy indirectly regulates synaptic function by controlling PKA-dependent phosphorylation of PSD scaffold proteins independent of their degradation. This function of autophagy requires the targeting of PKA R1α- and R1β-subunits to neuronal autophagosomes and can be triggered by starvation, a treatment that increases cAMP levels. cAMP causes dissociation of the PKA holoenzyme and exposes PKA R1 subunits for autophagosomal degradation. Loss of autophagy leads to the accumulation of PKA R1α- and R1β-subunits at synapses and impairs PKA signaling by sequestering the catalytic subunit of PKA. This leads to decreased phosphorylation of the PSD-confined scaffold protein involved in trafficking and endocytosis of synaptic GLUR1 receptors, resulting in an increase in GLUR1 at synapses.

Homeostatic synaptic plasticity is disrupted in autism spectrum disorders (ASD) (Tatavarty *et al*, 2020), a group of neurodevelopmental diseases characterized, among others, by dysfunctional autophagy (Lee *et al*, 2013). Several ASD-linked proteins have been found to be deregulated in their phosphorylation state in autophagy-deficient neurons in the current study, including SHANK3, SYNGAP1, DMXL2 and DPYSL2. Thus, it is possible, if not likely, that autophagy contributes to ASD etiology by regulating the PKA-dependent synaptic plasticity, among other mechanisms. Indeed, loss of autophagy has been associated with autistic-like synaptic pruning defects (Tang *et al*, 2014), while children with ASD are more likely to suffer from epilepsy (Besag, 2017), akin to the occurrence of seizures in mice conditionally lacking ATG5 reported here.

The work presented here identifies autophagy as a crucial regulator of PKA R1 levels in neurons, whereas protein levels of PKA R2 subunits are not affected by autophagy deficiency. These findings support the earlier study performed in non-neuronal cells, where R1α was reported to be localized to autophagosomes (Mavrakis *et al*, 2006) and are in line with the data suggesting dynamic cross-talk between autophagy and PKA (Cherra 3rd *et al*, 2010; Zhao *et al*, 2019). PKA R1α has also been observed in multivesicular bodies in mouse embryonic fibroblasts, suggesting the existence of alternative pathways for PKA R1 trafficking and degradation in cells (Day *et al*, 2011). What determines the specificity of degradation of PKA R1a/β by autophagy? The PKA R2 subunits are usually recruited to membranous compartments by AKAPs, whereas the PKA R1 subunits are mainly cytosolic, although their association with mitochondria has also been reported (Ilouz *et al*, 2012). We believe that cytosolic confinement of PKA R1 subunits predisposes them to autophagy by bulk sequestration of the cytoplasm. Recently, PKA R1α degradation by AKAP11-mediated selective autophagy was described to be required for the maintenance of mitochondrial metabolism in cancer cells (Deng *et al*, 2021). In our study, proteomic analysis of brains lacking ATG5 revealed no changes in AKAP11, suggesting that autophagy-dependent degradation of PKA R1 subunits in neurons may occur independently of AKAP11.

Increased surface localization of synaptic AMPA receptors is a known trigger of abnormal synchronous activity, a phenotype that may ultimately lead to epileptic seizures (Barker-Haliski & White, 2015; Joshi & Kapur, 2018; Guo & Ma, 2021; Wang *et al*, 2021). Whether the occurrence of spontaneous recurrent seizures in mice with autophagy deficiency in the excitatory forebrain neurons reported in the current study and previously (McMahon *et al*, 2012) is a direct consequence of dysfunctional PKA signaling needs to be determined in further studies. Based on our current data, we propose a model whereby autophagy contributes to neuronal excitability by regulating PKA-dependent phosphorylation of postsynaptic proteome, a function crucial for AMPA-mediated glutamatergic neurotransmission. Interestingly, nutritional interventions, such as a lipid-rich ketogenic diet, are a known modulator of neuronal excitability in epilepsy patients (D'Andrea Meira *et al*, 2019). Although the ketogenic diet is relatively efficient, it has some side effects, including leg cramps and digestive problems. The data presented here demonstrate therapeutic potential for the use of

FDA-approved autophagy-inducing drugs (i.e. metformin and spermidine) for the treatment of epilepsy. PKA signaling has been recently shown to restore synaptic responses in a mouse model of amyotrophic lateral sclerosis (Bączyk *et al*, 2020), a disease that is characterized by defective autophagy, among others (Chua *et al*, 2021). We believe that the components of the PKA signaling machinery should be explored as a potential target for the therapeutic restoration of synaptic function in other neurodegenerative conditions characterized by autophagy dysfunction, including Parkinson's disease and Alzheimer's disease.

Materials and Methods

Mouse models

All mice were housed in ventilated polycarbonate cages at standard 12/12 h day/night cycles. Food and water were provided *ad libitum*. All animal experiments are approved by the LANUV Cologne NRW and ethics committee and are conducted to the committee's guidelines (AZ 81-02.04.2020.A418, AZ 84-02.04.2016.A041, AZ 81-02.05.40.20.075, AZ 84-02.04.2016.A451). Conditional tamoxifen-inducible ATG5 and ATG16L1 KO mice (*Atg5*flox/flox: B6.Cg-Tg (CAG-Cre/Esr1*)5Amc/J) and *Atg5*flox/flox:*CamKIIα*-Cre mice were previously described (Negrete-Hurtado *et al*, 2020). Mice conditionally lacking ATG5 and/or ATG16L1 in inhibitory neurons were created by crossing *Atg5*flox/flox mice with *Slc32a1*-Cre line (#016962, The Jackson Laboratory), kindly provided by Prof. Matthew Poy (Johns Hopkins University School of Medicine, St. Petersburg, USA). Conditional ATG5 KO reporter mice were created by crossing both lines to *Ai9*(RCL-tdT) (tdTomato) line (The Jackson Laboratory) that was received from Prof. Matteo Bergami (CECAD, Cologne, Germany). *Atg5*flox/flox:*Slc32a1*-Cre and *Atg5*flox/flox:*CamKIIα*-Cre mice were used as knockouts (KO). In order to reduce the number of animals used for experiments (3R principle), mice carrying *Atg5*wt/wt:*Slc32a1*-Cre[tg], *Atg5*wt:wt/*Slc32a1*-Cre[wt], *Atg5*flox/wt:*Slc32a1*-Cre[wt], *Atg5*flox/wt: *CamKIIα*-Cre[wt] or *Atg5*flox/flox: *CamKIIα* -Cre[wt] genotypes were used as controls (wildtype [WT]; no phenotypical abnormalities were detected between all mentioned "WT" genotypes). Similarly, *Atg16L1*flox/flox:*Slc32a1*-Cre[tg] mice were used as knockouts (KO), whereas mice carrying *Atg16L1*wt/wt:*Slc32a1*-Cre[tg] and *Atg16L1*wt:wt/*Slc32a1*-Cre[wt], *Atg5*flox/wt:*Slc32a1*-Cre[wt] genotypes were used as WT. Primers used for mouse genotyping are shown in Appendix Table S1. Mice were genotyped for allocation into control (Cre negative) or experimental (Cre positive) groups. Within each group, all animals were generally used for experimental procedures, so no randomization was applied.

Neuronal cell culture

Cortical and hippocampal neurons from postnatal pups (P1-5) were isolated as previously described (Negrete-Hurtado *et al*, 2020) and plated on PDL-coated coverslips or dishes. Homologous recombination in neurons expressing *Atg5*flox:*CAG-Cre*[Tmx] was induced by applying 0.4 μM (Z)-4-hydroxytamoxifen (Sigma) immediately after plating. After 24 and 48 h, cells were treated with 0.2 and 0.4 μM of tamoxifen, respectively, during medium renewal. Ethanol was added to control neurons (WT) equal to tamoxifen.

Plasmid transfection of primary neurons

Neurons were transfected at DIV7 via calcium phosphate transfection using the ProFection Mammalian Transfection System-Calcium Phosphate Kit (Promega) following manufacturers' guidelines. In brief, plasmid DNA was mixed with 2 M $CaCl_2$, water and HEPES buffer (see Appendix Table S2). Neurons were covered with transfection solution in osmolarity-adjusted NeurobasalA medium (Gibco), washed and transferred back into their original medium. Experiments were done at DIV14-16 if not indicated differentially.

Nutrient deprivation of primary neurons

Neurons were starved by replacing regular culturing media with homemade, osmolarity-adjusted starvation media (1.8 mM $CaCl_2$, 0.8 mM $MgSO_4$, 5.3 KCl, 26.2 mM $NaHCO_3$, 117.2 mM NaCl, 1.0 mM NaH_2PO_4-H_2O, 5.5 mM D-Glucose). Cells were starved overnight (16 h) and harvested/ PFA fixated the following day. Bafilomycin A was supplemented in a concentration of 67 nM, H89 dihydrochloride was used in a 1 μM concentration in the media.

AAV-mediated transduction of primary neurons

AAVs (see Appendix Table S3) were added to the cell media at DIV5. For induction of GCAMP7[CamKIIα] expression, this AAV (ssAVV-9/2-mCaMKIIα-jGCaMP7f-WPREbGHp(A), Viral Vector Facility VVF) was added to the cell culture at DIV7.

Immunocytochemistry on cultured neurons

Neurons were fixed in 4% PFA/sucrose in phosphate-buffered saline (PBS) for 15 min at room temperature (RT) at DIV 14-16 and processed as described previously (Kononenko *et al*, 2017; see Appendix Tables S4 and S5 for the list of antibodies). Fixed neurons were imaged using either Zeiss Axiovert 200M microscope equipped with 40×/1.4 oil DIC objective and the Micro-Manager software (Micro-Manager1.4, USA) or with Leica SP8 confocal microscope (Leica Microsystems) equipped with a 63×/1.32 oil DIC objective and a pulsed excitation white light laser (WLL; ~ 80-ps pulse width, 80-MHz repetition rate; NKT Photonics).

Colocalization analysis

Colocalization of AMPA receptor subunit GLUR1 and postsynaptic density marker protein PDS95 were assessed in *Atg5*flox:*CAG-*Cre[Tmx] neurons in a semi-automated fashion using a macro-tool. For colocalization analysis an ROI was set in an area devoid of somata. Each channel was individually smoothened and binarized with a user-defined threshold before calculating the overlap area by dividing the overlap between PSD95 and GLUR1 by the total GLUR1 signal (custom written Image J script is available from authors upon request).

Analysis of pCREB-positive neurons after starvation

The percentage of pCREB positive neurons in different culture media was calculated from DAPI positive neurons (identified by morphology in DIC images).

STED imaging and analysis

STED imaging was done using a gSTED superresolution and confocal microscope (Leica Microsystems) equipped with 100× oil objective (HC PL APO 100×/1.4 Oil STED, Leica Microsystems) and a pulsed excitation white light laser (WLL; 80-MHz repetition rate; NKT Photonics) and two STED lasers (continuous wave at 592 nm, pulsed at 775 nm, MPBC). Within each independent experiment, samples were acquired with equal settings. Alexa Fluor 488 and ATTO 647N were excited using a pulsed WLL at 488 and 640 nm, respectively. Fluorescence signals were detected sequentially by hybrid detectors starting with the longer wavelength. Images were acquired with a scanning format of $1,024 \times 1,024$, eight-bit sampling, and 5 zoom. Pearson's coefficient analysis was done in PSD95 positive dendritic spines using ImageJ.

Live-imaging of cultured neurons using GLUR1-pHlourin

Neurons were imaged 7–8 days after transfection at DIV14-15 using Zeiss Axiovert 200M microscope (Observer. Z1, Zeiss, USA) equipped with 40×/1.4 oil DIC objective; a pE-4000 LED light source (CoolLED), and a Hamamatsu Orca-Flash4.O V2 CMOS digital camera. Time-lapse images were acquired every second using Micro-Manager software (Micro-Manager1.4, USA). The imaging chamber was connected to aVC-6 (six-channel valve controller, Warner Instrument Corporation) and plugged into a pump (Mini-Peristaltic Pump II, Harvard Apparatus) to ensure a constant media flow over the neurons. Note that all used media were osmolarity adjusted using D-Mannitol before the experiment. Neurons were imaged in imaging buffer (120 mM NaCl, 3.5 mM KCl, 0.4 mM KH_2PO_4, 20 mM N-Tris[hydroxyl-methyl]-methyl-2-aminoethane-sulphonicacid (TES), 5 mM $NaHCO_3$, 5 mM glucose, 1.2 mM Na_2SO_4, 1.2 mM $MgCl_2$, 1.3 mM $CaCl_2$, pH = 7.4) for 1 min to establish baseline GLUR1-pHlourin level. Afterwards, media conditions were switched to an acidic buffer (pH = 5.5) to quench the GLUR1-pHlourin signal from membrane-inserted receptors until a plateau was reached. For dequenching, the media was switched to a standard imaging buffer again. The total amount of GLUR1-pHlourin in the neurons was assessed by a media exchange to an alkaline buffer (NH_4Cl-buffer). To calculate the surface fraction of GLUR1-pHlourin receptors, 10 ROIs per neuron along the processes were chosen, and the mean fluorescence intensity signal was plotted over time using Image J (Plot Z-axis Profile). The background was subtracted for each single time point, and the mean of 30 images in the plateau phase of the single conditions was determined.

Purification of mouse autophagosomes (AVs)

The isolation of purified AVs was performed from 10 cortices and hippocampi of adult (postnatal day 60, P60) C57BL/6J male mice as described previously (Nikoletopoulou *et al*, 2017). Briefly, the tissue was homogenized in 10% sucrose, 10 mM Hepes and 1 mM EDTA (pH 7.3) by 20 strokes using a Dounce glass homogenizer. The material was then diluted in half volume of homogenization buffer (HB) (250 mM sucrose, 10 mM Hepes and 1 mM EDTA, pH 7.3) containing 1.5 mM glycyl-L-phenylalanine 2-napthylamide (GPN). After incubation at 37°C for 7 min, the material was centrifuged at 2,000 g for 2 min at 4°C, and the nuclear pellet was

discarded. The isolated post-nuclear supernatant was then loaded on discontinuous Nycodenz gradients that were centrifuged at 1,410,000 g for 1 h at 4°C, to remove the cytosolic, mitochondrial and peroxisomal fraction. The isolated autophagosomal and endoplasmic reticulum material was diluted with an equal volume of HB buffer and overlaid on Nycodenz-Percoll gradients for centrifugation at 72,000 g for 30 min at 4°C. After centrifugation, to remove the Percoll silica particles, the AVs' resulting interface was then diluted with 0.7 volumes of 60% Buffered Optiprep overlaid by 30% Buffered Optiprep and HB buffer. The Optiprep gradients were then centrifuged at 71,000 g for 30 min at 4°C. The collected AVs were diluted in three volumes of HB buffer and centrifuged for 30 min at 16,000 g at 4°C. The concentration of the purified isolated AVs was then measured by BCA, following the manufacturer's instructions. Purified AVs were treated with Proteinase K (PK) (20 ng/μl) on ice for 20 min, in the presence or absence of 1% Triton X-100, and then 4 mM of PMSF was added for 10 min on ice for PK inactivation. The samples were then centrifuged at 16,900 g for 10 min at 4°C, and the autophagosomal pellets were resuspended in Laemmli buffer, boiled for 5 min at 95°C and analyzed by Immunoblotting.

Immunoblotting

Mice were sacrificed at the age of 10–13-week via cervical dislocation. Brains were isolated, dissected, shock frozen in liquid nitrogen, and stored at −80°C till further use. Brain tissue was homogenized in radioimmunoprecipitation assay (RIPA) buffer (50 mM Tris pH 8.0, 150 mM NaCl, 1.0% IGEPAL CA-630, 0.5% Sodium deoxycholate, 0.1% SDS) containing Protease Inhibitor (Roche) and Phosphatase Inhibitor (ThermoScientific) using a Wheaton Potter-Elvehjem Tissue Grinder. Primary neurons, and NSC34 (CLU140, Cedarlane, provided by Prof. B. Wirth) cells were harvested in RIPA buffer containing Protease Inhibitor (Roche) and Phosphatase Inhibitor (ThermoScientific) using a cell scraper. Samples were sonicated and incubated on ice for 45 min. Lysates were centrifuged at 16.2 x g for 20 min at 4°C and supernatant concentration was assessed using the Bradford assay (Sigma). 10–20 μg of protein per sample was loaded onto SDS-page gels for protein separation. Proteins were transferred to Nitrocellulose or methanol-activated PVDF membranes (LC3). Membranes were blocked for 1 h with 5% skim milk (or BSA) in TBS (20 mM Tris pH = 7.6, 150 mM NaCl) containing 1% Tween (TBS-T) before incubation with the primary antibodies overnight at 4°C (see Appendix Table S4). The next day, the membranes incubated with secondary HRP-tagged secondary antibody (see Appendix Table S5) for 1 h at RT. Protein levels were visualized using an ECL-based autoradiography film system for documentation. Analysis was done using the Gel Analyzer plugin from Image J. For quantification, protein levels were always first normalized to the loading control and then the levels in the KO were normalized to the WT set to 100%. The same lysates were run in parallel to detect proteins of similar molecular weight, which were always first normalized to their respective loading controls before protein amounts were calculated.

Behavioral analysis

The SmithKline, Harwell, Imperial College, Royal Hospital, Phenotype (SHIRPA) test was performed to determine behavioral or

motoric alterations in WT and conditional ATG5-deficient mice (Hatcher *et al*, 2001). The mice were weighed and placed in a glass beaker (15 cm diameter, 19 cm height) for 2 min to determine their general health status. During this time, the activity of the mice was categorized (0– inactive, 1– active, 2– excessive active), the number of rears (Rearing) counted, and potential tremors, defecation, urination, lacrimation observed (0– no, 1– yes) and palpebral closure ranked (0– eyes open, 1– eyes closed). Afterwards, the mice were transferred into an arena (55 cm × 33 cm, 18 cm height) in which the floor was subdivided into uniform squares to observe alterations in locomotion. Transfer arousal (0– more than 5 s freezing, 1– brief freeze followed by movement; 2– immediate movement), gait (0– fluid/normal, 1– lack of fluidity/abnormal, 2– no data), pelvic elevation during motion (0– less than 5 mm, 1– more than 5 mm, 2– no data), tail elevation (0– dragging, 1– horizontal extension, 2– elevated, 3– no data) and the total number of squares passed during 1 min was noted. After 1 min, the touch escape was measured (0– none, 1– response to touch, 2– flees before touch) and the response to a loud, spontaneous noise was measured and ranked from 0 to 2 (0– no response, 1– Preyer reflex, 2– reaction in addition to Preyer reflex). To test the reflexes, the mice were held on to their tails and the trunk curl and limb grasping reflexes were assessed (0– no, 1– yes). Additionally, the righting reflex was observed (0– Absent, 1– Present) as well as the Corneal reflex using a cotton swap (0– no, 1– blink), tail pinch reflex (0– no, 1– yes) when holding the mice by the neck. During all the test procedure, the vocalization (0– no, 1– yes) and the biting evidence (0– no, 1– yes) were scored.

Electrocorticogram recordings

Telemetric electrocorticogram analyses were performed using implantable radio transmitters (models TA11EA-F10 or TA11ETA-F10, DataSciences International). Adult (at least 3 months old) male mice received 0.05 mg/kg buprenorphine (subcutaneously) for analgesia and were anesthetized with 1.5–2% isoflurane in 100% oxygen. Midline skin incisions were made on the top of the skull and in the neck. The transmitter body was implanted subcutaneously. The tips of the leads were placed 2 mm posterior to bregma and 1.8 mm right to the midline for the recording electrode, and 1 mm posterior to lambda and 1–2 mm left to the midline for the reference electrode. The electrodes were fixed with dental cement. Radio transmitters allowed simultaneous monitoring of electrocorticogram and motor activity in undisturbed, freely moving mice housed in their home cages. Telemetry data and corresponding video data were recorded 48–72 h after surgery and were stored digitally using Ponemah software (Data Sciences International). Electrocorticogram recordings lasted over 50 h, sampled at 500 Hz, with continuous video recording.

Recording of network activity of primary neurons using microelectrode arrays (MEA) system

Cortico-hippocampal neurons from postnatal *Atg5*flox:flox mice were isolated as described before (Kononenko *et al*, 2017) and plated in 24-well plates with gold electrodes on epoxy (24W700/100F-288, Multi Channel Systems). At DIV5, the KO was induced by transduction with *CamKIIα*-Cre (AAV9.CamKII.HI.eGFP-Cre.WPRESV40, Penn Vector Core). *CamKIIα*-eGFP (AAV9.CamKII0.4.eGFP.WPRE.rBG, Penn Vector Core) was used for the control group. MEA recordings were

acquired at DIV15 using the Multiwell-Screen software of the Multiwell-MEA-System (Multi Channel Systems). Recordings were taken for 3 min with a sampling rate of 20,000 Hz and automatic threshold estimation. The analysis was performed with the Multiwell-Analyzer software (Multi Channel Systems) using default parameters if not otherwise stated. Per well, the best channel electrode was selected for analysis. A well was considered active when at least three active electrodes were detected in the well (out of 12).

Immunohistochemical analysis of brain sections

Mice at 12–15-week were euthanized by an overdose of 1.2% ketamine, and 0.16% xylazine in PBS (i.p., 10 µl per 10 g body weight) and transcardial perfusion was performed as previously described (Kononenko *et al*, 2017). Brains were carefully dissected and postfixed in 4% PFA overnight before being processed for immunohistochemistry as previously described (Kononenko *et al*, 2017). Corresponding horizontal 40 µm sections from WT and KO littermates were washed three times in PBS (3 × 5 min each). Sections were blocked with 10% normal goat serum (NGS) or normal donkey serum (NDS) in 0.5% PBS-T for 1 h at RT. Primary antibodies (see Appendix Table S4) were incubated in sections in 3% NGS/NDS and 0.3% PBS-T overnight at 4°C. Sections were washed three times 10 min in 0.3% PBS-T before incubation in fluorescence-labeled secondary antibodies in 3% NGS/NDS and 0.3% PBS-T for 1 h at RT protected from light (see Appendix Tables S4 and S5). The sections were imaged at a Leica SP8 confocal microscope (Leica Microsystems) equipped with a 63×/1.32 oil DIC objective and a pulsed excitation white light laser (WLL; ~ 80-ps pulse width, 80-MHz repetition rate; NKT Photonics).

3D-analysis and reconstruction

Samples were scanned using Plan-Apochromat 63×/1.32 Oil DIC objective at a resolution of 1,024 × 1,024 pixels with 8-bit sampling in sequential scanning frame-by-frame mode. Single optical sections were acquired using identical acquisition settings, with the pinhole of 1 Airy Unit. Stacks of 8–29 optical sections yielded voxel dimensions between 100 and 300 nm for the X, Y and Z planes. 3D reconstructions were generated with Amira Software 2020.2 (Thermo Fisher Scientific). First, the surface area of the bassoon-positive synaptic contacts was reconstructed using the Amira segmentation editor. Bassoon/PRK R1α-positive contacts were defined by color-coding the surface of PRK R1α cells found within 250 nm from bassoon-positive varicosities. Subsequently, the surface of '250-nm-distant' PRK R1α-positive voxels was mapped onto Bassoon-positive contact using the "surface distance" tool and plotted as a histogram.

Cresyl-violet staining

Horizontal brain sections were obtained from perfused 13-week-old Atg5flox:Slc32a1-Cre mice and processed for cresyl violet staining as previously described (Kononenko *et al*, 2017).

NSC34 cells

Cells (CLU140, Cedarlane) were maintained in DMEM medium (GIBCO), supplemented 10% FCS (Sigma), 1% Pen Strep (Gibco),

1% MEM NEAA (Gibco). NSC34 cells were identified by their polarized morphology. To induce autophagy by Torin1, the media was supplemented with 250 nM Torin1 or exchanged with starvation media (1.8 mM $CaCl_2$, 0.8 mM $MgSO_4$, 5.3 KCl, 26.2 mM $NaHCO_3$, 117.2 mM NaCl, 1.0 mM NaH_2PO_4-H_2O, 5.5 mM D-Glucose). To block lysosomal degradation 67 nM Bafilomycin A was added in the last 4 h before harvesting for immunoblot analysis.

Immunogold labelling on brain sections

Mice were perfused with warm Ringer solution, followed by 4% PFA before the brains were sliced at a vibratome (400 μm). Slices were briefly stained with 0.2% methylene blue in PBS buffer. Small blocks with visible CA1 pyramidal cell layer and adjacent Stratum Radiatum were cut out by the razor and placed into the 2.3 M sucrose in 0.1 M PB solution for 24 h at 4°C. Following sucrose infiltration, blocks were placed at pins and plunged frozen in the liquid Ethan. Ultrathin (80 nm) cryosections were collected and thawed at sucrose drop (as described), placed at EM grids, blocked and washed in PBS supplemented with 1% BSA and 0.1% glycine, stained with R1 alpha or R1 alpha/beta antibodies 1:50. Following secondary antibody labelling 1:50 (12 nm gold goat anti-rabbit antibodies [Dianova]), ultrathin sections were embedded and contrasted with 3% Tungstosilicic acid hydrate (w/v) in 2.8% polyvinyl alcohol (w/v), dried and imaged in Zeiss 900 transmission electron microscope. Images of CA1 Stratum radiatum were taken without prior knowledge of genotype or antibody labelling conditions. The reference area of subneuropil structures was determined by superimposing a grid over the neuropil images (volume fraction estimation). The number of gold particles found at those structures was normalized to the volume fraction of corresponding structures in the neuropil. No immunogold labelling was detected in samples where the PKA R1-α/β antibody was omitted (negative control). The preparation of neurons for postsynaptic density thickness detection was described previously (Negrete-Hurtado et al, 2020). Electron micrographs were taken with a JEM-2100 Plus Electron Microscope (JEOL), Camera OneView 4K 16 bit (Gatan), and software DigitalMicrograph (Gatan). The postsynaptic density of the ultrathin section (70 nm) was measured using Image J.

Co-immunoprecipitation experiments

For immunoprecipitation experiments, 20 μl Dynabeads Protein G (Thermo Fischer Scientific) were coated with 2 μg antibody targeting the protein of interest and corresponding IgG as a negative control see Appendix Tables S4 and S5. Therefore, the bead's storing solution was replaced by 100 μl PBS, and 2 μg of antibody was added. The beads were incubated with the antibody for 2–3 h at 4°C on a shaker before washing once with 200 μl PBS to remove excess antibodies. Neurons were harvested/ tissue was homogenized using a Wheaton Potter-Elvehjem Tissue Grinder in Co-Immunoprecipitation (Co-IP) buffer (50 mM Tris-HCl pH = 7.4, 1% NP-40/Igepal, 100 mM NaCl, 2 mM $MgCl_2$) supplemented with Proteinase Inhibitor (Roche) und Phosphatase Inhibitor (ThermoScientific). Lysates were sonicated, incubated on ice for 45 min, and subsequently centrifuged at 13,000 for 20 min at 4°C. Protein concentration was assessed using Bradford assay (Sigma). An equal amount of protein was added to the beads coated with antibodies against the protein of interest and control IgG for overnight incubation at 4°C. The next day, lysates were removed, and beads were washed 3 times with Co-IP buffer before they were dissolved in 20 μl Co-IP buffer and 20 μl 4 s SDS buffer and boiled at 95°C for 5 min. Precipitation of proteins was detected via SDS-page gel.

FLIM-imaging of PKA signaling at synapses

To detect PKA signaling at the PSD Atg5flox:CAG-Cre[Tmx] neurons were transfected with AKARet-PSD plasmid (Addgene plasmid #114732) at DIV7. Live-cell FLIM imaging was done at DIV15 using a gSTED superresolution and confocal microscope (Leica Microsystems) equipped with a 63× water objective (HC PL APO 63×/1.2W CORR CS2, Leica Microsystems) and a pulsed excitation white light laser (WLL; 40-MHz repetition rate; NKT Photonics) and a live-cell imaging chamber to maintain the temperature at 37°C. The white light laser was used at 488 nm to excite the donor of the FRET sensor. The fluorescence lifetime images were acquired until the brightest pixel reached 1,000 photons. Control images were acquired before 100 μM IBMX and 50 μM Forskolin was applied to the media. For lifetime analysis, 10 ROIs outlining the PSDs of one neuron were averaged for control and each time point and the lifetime of the control measurement was subtracted from the different time point values. Analysis was done with the LASX FLIM/FCS software (version 3.5.6, Leica Microsystems). The changes in the lifetime are displayed over time.

Live-imaging of cultured neurons using GCAMP7 imaging

Calcium imaging experiments using GCAMP7[CamKII] (ssAVV-9/2-mCaMKIIα-jGCaMP7f-WPREbGHp(A), Viral Vector Facility VVF) were performed in Atg5flox:Ai9 WT and KO primary cortico-hippocampal neuronal cell culture. The KO was induced as described above. Live-cell imaging and stimulation were performed at DIV15-16 using Zeiss Axiovert 200M microscope (Observer. Z1, Zeiss, USA) equipped with 10×/0.3 EC Plan-Neofluar objective; a pE-4000 LED light source (CoolLED), and a Hamamatsu Orca-Flash4.O V2 CMOS digital camera. Neurons were imaged in an osmolarity adjusted imaging buffer described previously (Kononenko et al, 2013; 120 mM NaCl, 3.5 mM KCl, 0.4 mM KH_2PO_4, 20 mM N-Tris[hydroxy-methyl]-methyl-2-aminoethane-sulphonic acid [TES], 5 mM $NaHCO_3$, 5 mM glucose, 1.2 mM Na_2SO_4, 1.2 mM $MgCl_2$, 1.3 mM $CaCl_2$, pH 7.4), and time-lapse images were taken within a 1-s interval. For electrical field stimulation, neurons were stimulated four times with 100 action potentials (100 AP) in a 3-s interval at 100 Hz using an RC-47FSLP stimulation chamber (Warner Instruments). Coverslips with Atg5:CamKIIα-Cre and Atg5flox:Slc32a1-Cre neurons were only stimulated once and were allowed to rest for 5 min before the buffer was supplemented with 10 μM CNQX for 5 min before imaging. WT neurons transfected with GCAMP7[CamKIIα] (ssAVV-9/2-mCaMKIIα-jGCaMP7f-WPREbGHp(A), Viral Vector Facility VVF) were incubated with 10 μM H89 in DMSO or DMSO as a vehicle for 20 min before imaging. For analysis, neuronal cell bodies were chosen as ROI, and the GCAMP7 fluorescence response to the stimulus was plotted over time using Image J (Plot Z-axis Profile). Baseline fluorescence value was subtracted after background subtraction, and the traces were normalized to the first peak to visualize the facilitation. The 1st and 4th

peak differences was calculated and presented in the bar graphs. Experiments with 2 and 0 mM extracellular Ca^{2+} were performed using HEPES-based imaging buffer (in mM): 152 NaCl, 2.5 KCl, 10 glucose, 10 HEPES, 2 $CaCl_2$ (or 0 mM), 1 $MgCl_2$, pH 7.4.

Stereotactic injections

Stereotactic injections were performed on 10-week-old ATG5flox/flox mice, injected with *CamKII*-eGFP (AAV9.CamKII0.4.eGFP.W-PRE.rBG, Penn Vector Core) as control or *CamKII*-eGFP-Cre (AAV9.CamKII.HI.eGFP-Cre.WPRESV40, Penn Vector Core) to induce acute ATG5 deletion in layer II/III pyramidal neurons for electrophysiological experiments (Fig 7S and T). For experiments in *Atg5*flox/flox:Ai9 (KO) and *Atg5*wt/wt:Ai9 (WT) mice *CamKIIα*-Cre (ssAAV-9/2-mCaMKIIα-iCre-WPRE-hGHp(A)) was injected into the hippocampus (Fig 7C–F). For injections, mice were weighed and anesthetized with a mixture of Ketamine (100 mg/kg)/ Xylazine (20 mg/kg)/ Acepromazine (3 mg/kg) and placed in a stereotactic frame when fully asleep. A local painkiller was injected subcutaneously at the operation field. The skin was opened, and the skull was cleaned using NaCl. Point injection (AP from Bregma: −1.82 mm, LM: +3.8 mm) was identified using Bregma and Lambda for navigation. For injection, a small hole was drilled in the skull, and a 1 μl Hamilton syringe filled with the corresponding virus was lowered to the depth of −4.25 mm to inject 150 nl over 5 min. This process has been repeated at a depth of −3.5 mm to ensure sufficient virus-mediated transfection of neurons. Afterwards, the skull was rehydrated, the wound closed, and the mice were given a dose of carprofen to reduce postsurgical pain (s.c, 5 mg/kg) and 500 μl 5% glucose solution subcutaneously to enhance postoperative recovery.

Measurements of AMPAR currents using perforated patch configuration and analysis

Experiments were performed on brain slices containing the perirhinal cortex from 12-week-old *Atg5*flox:flox mice, which were stereotactically injected either with a control virus AAV expressing eGFP or with *CamKIIα*-Cre-eGFP AAV (see above). Animals were kept under standard laboratory conditions, with tap water and chow available *ad libitum*, on a 12 h light/dark cycle. The animals were lightly anesthetized with isoflurane (B506; AbbVie Deutschland GmbH and Co KG, Ludwigshafen, Germany) and decapitated. Coronal slices (300 μm) were cut with a vibration microtome (VT1200 S; Leica, Germany) under cold (4°C), carbogenated (95% O_2 and 5% CO_2), glycerol-based modified artificial cerebrospinal fluid (GaCSF; Ye *et al*, 2006). GaCSF contained (in mM): 244 glycerol, 2.5 KCl, 2 $MgCl_2$, 2 $CaCl_2$, 1.2 NaH_2PO_4, 10 HEPES, 21 $NaHCO_3$, and 5 Glucose adjusted to pH 7.2 with NaOH. Brain slices were transferred into carbogenated artificial cerebrospinal fluid (aCSF). First, they were kept for 20 min in a 35°C 'recovery bath' and then stored at room temperature (24°C) for at least 30 min prior to recording. aCSF contained (in mM): 125 NaCl, 2.5 KCl, 2 $MgCl_2$, 2 $CaCl_2$, 1.2 NaH_2PO_4, 21 $NaHCO_3$, 10 HEPES, and 5 Glucose adjusted to pH 7.2 with NaOH. Slices were transferred to a recording chamber (~ 3 ml volume) and continuously superfused with carbogenated aCSF at a flow rate of ~ 2 ml·min^{-1}. Whole-cell voltage-clamp recordings of individual layer II/III pyramidal neurons were

performed at ~ 32°C. Neurons were visualized with a fixed stage upright microscope (BX51WI; Olympus, Tokyo, Japan) equipped with infrared differential interference contrast optics and fluorescence optics. Layer II/III pyramidal neurons were identified by their anatomical location and eGFP-fluorescent label. Electrodes with tip resistances between 3 and 5 MΩ were fashioned from borosilicate glass (0.86 mm inner diameter; 1.5 mm outer diameter; GB150-8P; Science Products) with a vertical pipette puller (PP-830; Narishige, London, UK). All recordings were performed using a dSEVC (discontinuous single-electrode voltage-clamp) amplifier (SEC-05X, npi Electronics GmbH, Tamm, Germany) controlled by the program Patch-Master (version 2.32; HEKA). AMPA-R currents were recorded in discontinuous voltage clamp mode. The switching frequency and duty cycle of the amplifier were set to 40–50 kHz and 1/4 (current injection/potential recording), respectively Data were low-pass filtered at 3 kHz with a four-pole Bessel filter and sampled at 10 kHz. Data were recorded using a micro1410 data acquisition interface and Spike 2 (version 7; both from CED, Cambridge, UK). Patch pipettes were filled with the following (in mM): 140 KCl, 10 HEPES, 0.1 EGTA, 5 MgCl2, 5 K-ATP, 0.3 Na-GTP, adjusted to pH 7.3 with KOH. Neurons were voltage clamped at −70 mV. The calculated liquid junction potential (3.6 mV) was compensated. To isolate AMPA receptor-mediated PSCs, GABAergic inhibitory PSCs were blocked with picrotoxin (100 μM; Sigma) and NMDA receptor-mediated PSCs were blocked with DL-2-amino-5-phosphonopentanoic acid (D-AP5; 50 μM; Sigma). The AMPA-R PSC frequency and amplitude were determined from a 1 min interval after the recording had stabilized (~ 10 min after wash-in of picrotoxin/D-AP5). The data were digitally filtered offline using the smooth (1 msec time period) and the DC remove (500 msec time period) functions in the Spike2 software (CED, Cambridge, UK). Data analysis was performed with Spike2 (version 7; Cambridge Electronic Design Ltd., Cambridge, UK) and the Pandas software library for Python 3.x (https://pandas.pydata.org/). Estimation statistics and plots were generated with the DABEST library for Python 3.x. The final figure was made with Adobe Illustrator 2022 (Adobe, San Jose, CA, USA) running on an Apple Macintosh.

Fluorescence-activated cell sorting (FACS) of isolated neurons

Neurons for FACS sorting were isolated from 3-week-old *Atg5*flox:*CamkIIα*-Cre:*Ai9* and *Atg5*flox:*Slc32a1*-Cre:*Ai9* reporter mice. Mice were transcardially perfused with ACSF to remove blood cells. Isolated brains were dissected in HibernateA (HA, Gibco) and the cortex, hippocampus and striatum were isolated and transferred into a fresh dish containing HABG (Hibernate-A, 2% B27, 1% GlutaMax). The tissue was cut into pieces and digested in activated Papain (Worthington) for 40 min at 37°C. Afterwards, tissue pieces were transferred back into fresh HABG. They were homogenized with a fire-polished Pasteur pipette (triturate approximately 10 times in 1 min). The cell suspension was applied on an OptiPrep®Density Gradient Medium (Sigma) centrifuged at 800 *g* for 15 min at 22°C to force cell type separation. Neuron-enriched fractions were maintained for further processing. Gradient material was diluted with 10 ml HABG and cells were pelleted down at 3,000 *g* for 3 min at 22°C to clean cell suspension from debris contaminations. This step was repeated once before the cells were resuspended in NBA supplemented with 2% B27. To obtain purified lysates from

autophagy-deficient neurons, cells in suspension were stained with DAPI and DRAQ5 (see Appendix Tables S4 and S5). Cell sorting was performed using BD FACSAria Fusion IIu and BD FACSAria IIIu with FACSDiva 8.0.1 software. Neurons were sorted at 4°C using a 100 μm nozzle and sheath pressure was set at 20 psi. 0.9% NaCl was used as sheath fluid. The tdTomato highly positive/ DAPI negative/ DRAQ5 positive cell population was selected. Cells were collected in chilled 1.5 ml Eppendorf tubes containing DPBS. After sorting, the cells were centrifuged at 3,000 g for 3 min and lysed in buffers depending on subsequent analysis.

RNA sequencing

RNA of FACS sorted neurons were isolated using the RNeasy® Plus Micro Kit (Qiagen) following manufacturer's instructions. Isolated RNA was forwarded to RNA sequencing. Library preparation was performed with the NEBNext® Ultra Directional RNA Library Prep Kit for Illumina. The first step involves the removal of ribosomal RNA using biotinylated target-specific oligos combined with rRNA removal beads from 1 μg total RNA input. The NEBNext® rRNA Depletion Kit (Human/Mouse/Rat) depletes samples of cytoplasmic rRNA. Following purification, the RNA is fragmented into small pieces using divalent cations under elevated temperatures. The cleaved RNA fragments are copied into first-strand cDNA using reverse transcriptase and random primers, followed by second-strand cDNA synthesis using DNA Polymerase I and RNase H. These cDNA fragments then have the addition of a single 'A' base and subsequent ligation of the adapter. The products are purified and enriched with PCR (20 μl template, 15 cycles) to create the final cDNA library. After library validation and quantification (Agilent Tape Station), equimolar amounts of the library were pooled. Pools of 4–6 libraries were quantified using the Peqlab KAPA Library Quantification Kit and the Applied Biosystems 7900HT Sequence Detection System and sequenced on a NovaSeq 6000 S4 flowcell 2x100bp.

Bioinformatic analysis of RNA sequencing raw data

Illumina adapters were clipped off the raw paired-end reads using cutadapt v2.10 (Martin, 2011) with standard parameters and a minimum read length of 35 base pairs after trimming (shorter reads were discarded).

For read 1, the adapter sequences trimmed were AGATCGGAA GAGCACACGTCTGAACTCCAGTCA, AGATCGGAAGAGCACACGT CTGAAC, TGGAATTCTCGGGTGCCAAGG, AGATCGGAAGAGCACA CGTCT, CTGTCTCTTATACACATCT, and AGATGTGTATAAGAG ACAG.

For read 2, the sequences were AGATCGGAAGAGCGTCGTG TAGGGAAAGAGTGT, AGATCGGAAGAGCGTCGTGTAGGGA, TGG AATTCTCGGGTGCCAAGG, AGATCGGAAGAGCACACGTCT, CTGT CTCTTATACACATCT and AGATGTGTATAAGAGACAG.

Transcript quantification

Transcript abundance was quantified using kallisto v0.46.1 (Bray et al, 2016). The transcriptome index was built by kallisto index from file Mus_musculus.GRCm38.rna.fa of Ensembl release 100. Subsequently, the adapter-trimmed RNA-seq reads were matched

against the index using kallisto quant with standard parameters and 100 bootstrap samples (−b 100). Transcript abundances (= TPMs, = estimated Transcripts Per Million) were extracted from the primary output of kallisto using package tximport v1.16.1 of the Bioconductor v3.11 (Huber et al, 2015) software project, in an environment of the R v4.0.0 programming language. In the same environment, Ensembl transcript ids were mapped to Ensembl gene ids and gene symbols, using package biomaRt v2.44.4 to access the Ensembl v100 database. A table containing the gene ids, gene symbols, and kallisto TPMs was output as kallisto_tx_abundance.xlsx (141,450 transcripts). In table kallisto_tx_abundance_1TPM.xlsx, transcripts represented by < 1 TPM were filtered out (see Dataset EV2). The P-value of the Kallisto gene counts was calculated, and all significant hits were forwarded to analysis. The means were calculated between the genotypes and the genes sorted by the difference between WT and KO. The dataset was divided into up- and down-regulated hits and both datasets were analyzed using Enrichr (Ma'ayan Lab, Icahn School of Medicine at Mount Sinai, New York) gene set analysis. Results from ChEA 2016 analysis are presented as Clustergrams. For downstream gene-based analysis, the TPM values of transcript ids associated with the same Ensembl gene id were summed up. This resulted in 53,028 unique Ensembl gene ids in the full matrix and 23,669 unique Ensembl gene ids in the 1TPM-filtered matrix. The Ensembl ids were associated with 52,263 unique gene symbols in the full matrix and 23,380 unique gene symbols in the filtered matrix. To resolve cases where > 1 Ensembl gene id mapped to the same symbol, we discarded Ensembl gene ids that were not represented in the Ensembl v100 genome annotation file Mus_musculus.GRCm38.100.gtf. (Note that unrepresented Ensembl gene ids were not removed if they did not cause a mapping conflict. As all unrepresented ids came from PATCH contigs rather than from the canonical chromosomes, this may be an issue. On the other hand, these contigs had been part of the kallisto index used and thus have had an influence on the mapping process, so they should be represented in the output.) After the removal of 873 Ensembl gene ids due to conflicts, the final number of genes represented in the full matrix was 52,155, and 23,319 in the 1TPM-filtered matrix. In addition to the TPM values, kallisto also outputs estimated read counts per transcript. We converted these to read counts per gene by summing over associated transcripts as above, and retaining the same genes as in the gene-collapsed TPM matrices.

Differential gene expression analysis

We used the R package sleuth v0.30.0 (Pimentel et al, 2017) for differential gene expression, because sleuth is explicitly designed to work with kallisto output. Because the experimental samples had been sequenced in two batches, we employed an additive linear model with categorical factors Batch and Genotype. File newDGE_sleuth_BG_reproduced.xlsx reports the result of the sleuth analysis for model coefficient Genotype, that is, for the effect of genotype state (WT or KO) on transcript expression, corrected for batch membership of the samples. Sleuth was configured to run Wald tests on the coefficients of the linear model and to not aggregate the P-values from the individual transcripts contributing to a gene's expression. Therefore, a given Ensembl gene id is usually represented in more than one row of the table. The original sleuth

output column names "b" (effect strength of the model coefficient), "pval" (*P*-value = probability of the effect being equal to zero), and "qval" (FDR adjusted *P*-value using the Benjamini-Hochberg procedure) have been replaced by "logFoldChange", "*P*-value", and "FDR". (Note that the effect strength "b" is only roughly comparable to the natural logarithm of fold change and that it's not even clear whether in sleuth v0.30.0 the definition has not already been changed to log2—see https://github.com/pachterlab/sleuth/issues/59).

High content screening microscopy

Cells were isolated from adult 12–13-week-old mice as described for FACS sorting. Afterwards, the cells were resuspended in supplemented NBA medium, were seeded 100 μl/well in clear 96-well plates (Greiner #655896) and incubated for 3 h (37°C, 5% CO_2) before stimulation. Using an electronic 8-channel pipette (Eppendorf) at low dispense speed, the cells were stimulated for 15 min. The stimulant compound was prepared 10-fold concentrated in 12.5 μl of PBS (PAA #H15-002) in 96-well V-bottom plates (NerbePlus, #10-111-000). Half of the media (50 μl) was removed from the wells in the cell culture plate, mixed with a stimulant in the V-bottom plate, and added back to the well. Negative controls were stimulated with the vehicle only. The cells were fixed by adding 100 μl 8% PFA (4% final) for 10 min followed by 2× wash with 100 μl PBS. Then the cells were blocked and permeabilized with 50 μl normal goat serum blocking (NGSB) for 1 h at room temperature. Afterwards, the cells were incubated with 30 μl primary antibodies diluted in 1% BSA overnight at 4°C. Rinsed 3× with 100 μl PBS for 10 min each and were incubated with 50 μl secondary antibodies diluted 1:1,000 in PBS for 1 h at room temperature in the dark and rinsed 3× with 100 μl PBS for 10 min each (see Appendix Tables S4 and S5). Finally, the wells were filled with 200 μl PBS and sealed with aluminum. For imaging, a CellInsight CX7 LZR (ThermoFisher Scientific) microscope with a laser light source. We used the 20× objective and acquired images of 1,024 × 1,024 pixels. Image analysis was performed using the Cellomics software package. Briefly, images of tdTomato stainings were background corrected (low pass filtration), converted to binary image masks (fixed threshold), and segmented (geometric method). Inhibitory neurons were then identified by appropriate object selection parameters such as size, circularity, and average tdTomato intensity. These image masks were then overlaid on images obtained at other fluorescence wavelengths to quantify signal intensities. To later determine spillover between fluorescence channels, three respective controls for each triple staining: (1) tdTomato alone, (2) tdTomato + antibody 1, and (3) tdTomato + antibody 2 were included. Single-cell data containing the raw fluorescence data of single cells from the Cellomics software was exported as spreadsheets and analyzed by open-source statistical language R. The raw fluorescence data of the controls were used to calculate the slope of best fit straight lines by linear regression, which were then applied to compensate. Compensated data were scaled to a mean value of 1 for the vehicle-stimulated cells to adjust for variability between experimental treatments. To visualize the data, we used two-dimensional probability density plots generated using R. For gating of subpopulations, we set thresholds at local minima of probability density plots.

cAMP assay

cAMP concentration in the hippocampus of autophagy-deficient mice was measured using the cAMP Direct Immunoassays Kit (Flourometric) from Abcam (ab138880) following the manufacturers' instructions. Hippocampi of *Atg5*flox:*CamKIIα*-Cre WT and KO mice were dissected at 12 weeks of age, snap-frozen and stored at −80°C. Hippocampi were weighted and homogenized in lysis buffer depending on tissue weight using a Wheaton Potter-Elvehjem Tissue Grinder (VWR). Insoluble material was removed by centrifugation before the supernatant was pipetted into the anti-cAMP coated 96-well plate. A standard with pre-defined cAMP concentrations was loaded in parallel. Total cAMP content was calculated using a set amount of HRP*-cAMP conjugate and HRP-dependent fluorescent substrate detected by a microplate reader at Ex/Em = 540/590 nm.

Proteome analysis using LC-MS/MS

For total proteome analysis *Atg5*flox:CAG-Cre^Tmx and *Atg16L1*flox:CAG-Cre^Tmx cultured cortico-hippocampal neurons were harvested at DIV15-16 in RIPA buffer and processed as described for Immunoblotting (see above). A total of 50 μg were forwarded for proteomic analysis using an in-gel digestion protocol for sample preparation. In brief, samples were loaded onto an SDS-PAGE gel and run for 1–2 cm. The whole running line was chopped into small pieces and transferred in a 1.5 ml Eppendorf tube. Samples were reduced (10 mM DTT) and alkylated (55 mM CAA). Digestion of proteins was done overnight using Trypsin (10 ng/μl 90% Trypsin) and LysC (50 mM). Peptides were extracted and purified using Stagetips. Eluted peptides were dried in vacuo, resuspended in 1% formic acid/4% acetonitrile and stored at −20°C prior to MS measurement. For proteome analysis of FACS-sorted neurons, the cells were pelleted and resuspended in SP3 lysis buffer (5% SDS in PBS). Chromatin was degraded using a Biorupter (10 min, cycle 30/30). The samples were reduced (5 mM DTT) and alkylated (40 mM CAA) and protein content was measured with the Pierce BCS protein assay. 20 μg were used for protein digestion according to the single-pot solid-phase-enhanced sample preparation (Hughes *et al*, 2019).

LC-MS/MS acquisition and data analysis

*Atg5*flox:CAG-Cre^Tmx cultured neurons
All samples were analyzed on a Q Exactive Plus Orbitrap (Thermo Scientific) mass spectrometer coupled to an EASY nLC (Thermo Scientific). Peptides were loaded with solvent A (0.1% formic acid in water) onto an in-house packed analytical column (50 cm—75 μm I.D., filled with 2.7 μm Poroshell EC120 C18, Agilent). Peptides were chromatographically separated at a constant flow rate of 250 nl/min using the following gradient: 4–5% solvent B (0.1% formic acid in 80% acetonitrile) within 1.0 min, 5–28% solvent B within 200.0 min, 28–50% solvent B within 28.0 min, 50–95% solvent B within 1.0 min, followed by washing and column equilibration. The mass spectrometer was operated in data-dependent acquisition mode. The MS1 survey scan was acquired from 300–1,750 *m/z* at a resolution of 70,000. The top 10 most abundant peptides were isolated within a 2.0 Th window and subjected to HCD fragmentation at a normalized collision energy of 27%. The AGC target was set to 5e5 charges, allowing a maximum injection time of

55 ms. Product ions were detected in the Orbitrap at a resolution of 17,500. Precursors were dynamically excluded for 40.0 s. Each sample was injected twice. *Data analysis*. All mass spectrometric raw data were processed with Maxquant (version 1.5.3.8) using default parameters. Double injections from each sample were combined in MaxQuant by naming them identically. MS2 spectra were searched against the Uniprot mouse reference proteome containing isoforms (UP000000589, downloaded at 26.08.2020), including a list of common contaminants. The target-decoy approach estimated false discovery rates on protein and PSM levels to 1% (Protein FDR) and 1% (PSM FDR), respectively. The minimal peptide length was set to 7 amino acids, and carbamidomethylation at cysteine residues was considered a fixed modification. Oxidation (M), Phospho (STY), and Acetyl (Protein N-term) were included as variable modifications. The match-between runs option was enabled. LFQ quantification was enabled using default settings.

Atg16L1flox:CAG-Cre^{Tmx} cultured neurons

Peptide digests were analyzed on a Q Exactive plus Orbitrap (Thermo Scientific) mass spectrometer coupled to an EASY nLC (Thermo Scientific). Samples were loaded onto an in-house packed analytical column (50 cm—75 μm I.D., filled with 2.7 μm Poroshell EC120 C18, Agilent). Peptides were separated at a 250 nl/min flow rate using 2 h runs with data-independent acquisitions (DIA) or 4 h runs with the data-dependent acquisition (DDA). The gradients were: (2 h) 3–5% solvent B (0.1% formic acid in 80% acetonitrile) within 1.0 min, 5–30% solvent B within 91.0 min, 30–50% solvent B within 17.0 min, 50–95% solvent B within 1.0 min, followed by washing with 95% solvent B for 10 min or (4 h) 4–5% solvent B (0.1% formic acid in 80% acetonitrile) within 1.0 min, 5–28% solvent B within 200.0 min, 28–50% solvent B within 28.0 min, 50–95% solvent B within 1.0 min, followed by washing with 95% solvent B for 10 min. DDA runs for spectrum library generation were acquired from each sample. MS1 survey scans were acquired at a resolution of 70,000. The top 10 most abundant peptides were isolated within a 2.0 Th window and subjected to HCD fragmentation with a normalized collision energy of 27. The AGC target was set to 5e5 charges, allowing a maximum injection time of 55 ms. Product ions were detected in the orbitrap at a resolution of 17,500. Precursors were dynamically excluded for 20.0 s. Sample runs were acquired in DIA mode using 10 variable windows covering the mass range from m/z 450 to m/z 1,200. MS1 scans were acquired at 140,000 resolution, and maximum IT restricted to 120 ms and an AGC target set to 5e6 charges. The settings for MS2 scans were 17,500 resolution, maximum IT restricted to 60 ms and AGC target set to 5e6 charges. The default charge state for the MS2 was set to 4. Stepped normalized collision energy was set to 27. All spectra were acquired in profile mode. *Data analysis*. An assay-specific hybrid spectrum library was generated in Spectronaut 13 (Bruderer *et al*, 2015) using DDA library runs, DIA sample runs, and a mouse sequence file (up000000589) downloaded from Uniprot. Spectronaut default settings were used for the analysis of the DIA runs. Protein identifications were filtered for *q*-values below 0.01, and normalized intensities were exported for subsequent statistical analysis in Perseus 1.6.1.1 (Tyanova *et al*, 2016). Intensities were transformed to log2 values, and the dataset was filtered for at least 3 out of 3 values in at least one condition. The remaining missing values were imputed with random values from the left end of the intensity

distribution (with 0.3 s.d., downshift 2 s.d.). Two runs were removed from the analysis since the projection in the principal component analysis was outside median plus/minus 4 times inter quartile range for component 1 or 2. Two sample Student's *T*-tests were calculated using permutation-based FDR estimation.

FACS-sorted neurons from Atg5flox:Slc32a1-Cre:Ai9 mice

The LCMS analysis approach was adjusted to handle low input volume. Samples were analyzed on a Q Exactive Exploris 480 (Thermo Scientific) mass spectrometer that was coupled to an Evosep ONE (Evosep) in the recommended "whisper" setup. Samples were loaded onto EvoTips following the manual instructions (Evosep). Peptides were chromatographically separated by the predefined "whisper 20 SPD" setup on a 58 min gradient on a PepSep 15 cm column with a 75 μm inner diameter filled with 1.9 μm Dr. Maisch resin. MS1 scans were acquired from 380 to 900 m/z at 45 k resolution. Maximum injection time was set to 60 ms and the AGC target to 100%. MS2 scans ranged from 400 to 880 m/z and were acquired at 45 k resolution with a maximum injection time of 84 msec and an AGC target of 1,000%. DIA scans covering the precursor range from 400–880 m/z were acquired in 15×30 m/z staggered windows resulting in 30 nominal 15 m/z windows after demultiplexing. All scans were stored as a centroid. *Data analysis*. Thermo raw files were demultiplexed and transformed to mzML files using the msconvert module in Proteowizard. MzML files were converted to dia file format in DIA-NN 1.7.15. A Mouse canonical Swissprot fasta file was converted to a Prosit upload file with the convert tool in encyclopedia 0.9.0 (Searle *et al*, 2018) using default settings: Trypsin, up to 1 missed cleavage, range 396–1,004 m/z, charge states 2^+ and 3^+, default charge state 3 and NCE 33. The csv file was uploaded to the Prosit webserver and converted to a spectrum library in generic text format (Gessulat *et al*, 2019). The resulting library (16,998 protein isoforms, 21,694 protein groups and 1,404,872 precursors was used in DIA-NN 1.7.15; Demichev *et al*, 2020) to search acquired data in double-pass mode. The applied settings were: Output will be filtered at 0.01 FDR, N-terminal methionine excision enabled, Maximum number of missed cleavages set to 1, Min peptide length set to 7, Max peptide length set to 30, Min precursor m/z set to 400, Max precursor m/z set to 1,000, Cysteine carbamidomethylation enabled as a fixed modification.

FACS-sorted neurons from Atg5flox:Slc32a1-Cre:Ai9

Samples were analyzed on a Q Exactive Exploris 480 (Thermo Scientific) mass spectrometer equipped with a FAIMSpro differential ion mobility device coupled to an EASY-nLC 1200 (Thermo Scientific). Samples were loaded onto an in-house packed analytical column (30 cm—75 μm I.D., filled with 2.7 μm Poroshell EC120 C18, Agilent). Peptides were chromatographically separated at a constant flow rate of 300 nl/min and the following gradient: initial 4% B (0.1% formic acid in 80% acetonitrile), up to 30% B in 74 min, up to 55% B within 8.0 min and up to 95% solvent B within 2.0 min, followed by a 6 min column wash with 95% solvent B. The FAIMS pro was operated at −47 V compensation voltage and electrode temperatures of 99.5°C for the inner and 85°C for the outer electrode. Identical HPLC settings were used for library generation, and sample runs.

Spectrum library generation by Gas-phase fractionation

Aliquots from each sample were pooled, and the pool was used for spectrum library generation by narrow window DIA of six 100 m/z gas phase fractions (GPF) covering the range from 400 to 1,000 m/z (Searle *et al*, 2020). The Orbitrap was operated in DIA mode. MS1 scans of the respective 100 m/z gas-phase fraction were acquired at 60 k resolution. Maximum injection time was set to 60 ms and the AGC target to 100%. MS2 scans of the corresponding 100 m/z regions were acquired in 24×4 m/z staggered windows resulting in 48 nominal 2 m/z windows after demultiplexing. MS2 settings were 30 k resolution, 60 ms maximum injection time and an AGC target of 100%. All scans were stored as a centroid.

Data independent acquisition of samples

MS1 scans were acquired from 390 to 1,010 m/z at 60 k resolution. Maximum injection time was set to 60 ms and the AGC target to 100%. MS2 scans ranged from 300 to 1,500 m/z and were acquired at 15 k resolution with a maximum injection time of 22 msec and an AGC target of 100%. DIA scans covering the precursor range from 400–1,000 m/z were acquired in 50×12 m/z staggered windows resulting in 100 nominal 6 m/z windows after demultiplexing. All scans were stored as a centroid. *Data analysis.* Thermo raw files were demultiplexed and transformed to mzML files using the msconvert module in Proteowizard. MzML files were converted to dia file format in DIA-NN 1.7.11.

Spectral library

A Mouse canonical Swissprot fasta file was converted to a Prosit upload file with the convert tool in encyclopedia 0.9.0 (Searle *et al*, 2018) using default settings: Trypsin, up to 1 missed cleavage, range 396–1,004 m/z, charge states 2^+ and 3^+, default charge state 3 and NCE 33. The csv file was uploaded to the Prosit webserver and converted to a spectrum library in generic text format (Gessulat *et al*, 2019). The resulting library (16,998 protein isoforms, 21,698 protein groups and 1,404,872 precursors) was searched in DIA-NN 1.7.11 (Demichev *et al*, 2020) with the 6 GPF runs to generate a project-specific library (6,275 protein isoforms, 6,523 protein groups and 26,215 precursors). The applied settings were: Output will be filtered at 0.01 FDR, N-terminal methionine excision enabled, the maximum number of missed cleavages set to 1, min peptide length set to 7, max peptide length set to 30, min precursor m/z set to 400, Max precursor m/z set to 1,000, cysteine carbamidomethylation enabled as a fixed modification.

Samples

Ten sample files were searched with DIA-NN 1.7.11 and the project library. In addition to the settings used for library generation, Rt dependent normalization was used.

Phosphoproteome analysis using LC-MS/MS

Experiments were performed with *Atg5*flox:*CamKIIα*-Cre and *Atg5*flox:*Slc32a1*-Cre WT/KO 12–14-week-old brain tissue. Brains from SILAC-labeled mice (Krüger *et al*, 2008), and ATG5 KO mice of both lines were homogenized using a Wheaton Potter-Elvehjem Tissue Grinder (VWR) in 6 M Urea/ 2 M Thiourea. Lysates were sonicated and centrifuged at maximum speed. The supernatant was forwarded to protein concentration assessment using Pierce™ 660 nm Protein Assay Reagent (Thermo Scientific™). Lysates of

ATG5 KO mice were mixed with brain lysates of isotope-labeled mice in a ratio of 1:1 (1 mg:1 mg). Samples were incubated with 10 mM DTT for 30 min at RT, followed by 45 min incubation with 55 mM IAA in the dark. Afterwards, samples were pre-digested with LysC in an enzyme:substrate ratio of 1:50 for 2 h. The samples were diluted three times with 50 mM ABC buffer to reach a concentration of 2 M Urea before LysC was added again in an enzyme:substrate ratio of 1:100 for overnight digestion at RT. The next day, desalting and phosphopeptide enrichment were performed. Experiments with acute brain slices of *Atg5*flox:*CamKIIα*-Cre WT and KO treated with the cAMP-inducing agent Forskolin were performed with 12–14 week old mice. The brain was isolated and chopped into 400 μm thick sections. The sections were washed with HBSS, transferred into media, and placed in the incubator for 1 h. Afterwards, they were treated with 50 μM Forskolin for 15 min before being washed with ice-cold PBS for albumin removal. The sections were snap-frozen and stored at −80°C till further use. On the day of the experiment, slices were homogenized in 1.5 ml 8 M Urea buffer using a Wheaton Potter-Elvehjem Tissue Grinder (VWR). The lysates were sonicated and centrifuged at 13,000 rpm for 10 min. Protein concentration was assessed using Pierce™ 660 nm Protein Assay Reagent (Thermo Scientific™) and 1 mg protein of each sample taken for the experiment. The samples were pre-digested in 5 mM TCEP, 27.5 mM CAA and LysC, in an enzyme:substrate ratio of 1:50 for 3 h at RT after vortexing. Afterwards, the samples were diluted to a concentration of 2 M Urea using 50 mM ABC buffer. Trypsin was added to an enzyme:substrate ratio of 1:100 and incubated overnight at RT. The next day, desalting and phosphopeptide enrichment were performed. The next day, after Trypsin digestion, the samples of both datasets were acidified with TFA (1:100 [v/v]) before 10 min centrifugation. Desalting of the samples was performed with 50 mg C_{18} SepPak®Vac cartridges (Waters™). Therefore, the columns were activated with 2 ml 100% CAN and washed three times with 1 ml 0.1% TFA before loading samples. Samples were washed three times with 1 ml 0.1% TFA prior to elution with 0.6 ml elution buffer (60% ACN, 0.1% TFA). 30 μg of the sample were taken, desalted, and stored on stage tips for total proteome analysis (described above) before the remaining sample was dried in a vacuum concentrator. TiO$_2$ Phosphopeptide extraction was performed using the High-Select™ TiO$_2$ Phosphopeptide Enrichment Kit (Thermo Scientific™) following the manufacturers' instructions. In brief, a lyophilised peptide sample was resuspended in 150 μl Binding/Equilibration Buffer, columns prepared using 20 μl Wash Buffer followed by 20 μl Binding/ Equilibration Buffer. The samples were run twice through the column before the column was washed with 20 μl Binding/ Equilibration Buffer followed by 20 μl Wash Buffer. Afterwards, the columns were washed with 20 μl of LC-MS grade water before the phosphopeptides were eluted from the column in a 50 μl Phosphopeptide Elution Buffer. Samples were dried immediately using a vacuum concentrator and subsequently resuspended in 15 μl resuspension buffer (5% FA and 2% ACN). Phosphopeptide samples were stored at −20°C until measurement.

LCMS data acquisition

Proteome samples were eluted from stage tips with elution buffer (60% ACN, 1% ammonia), dried in a vacuum concentrator and resuspended in 12 μl resuspension buffer. Proteome and phosphoproteome samples were measured on a Thermo Orbitrap Eclipse

mass spectrometer with an AIMS interface coupled to a Thermo EASY-nLC system. Each sample was measured in a 90 min reverse phase separation using two FAIMS CVs −45 and −65 V. *Data analysis*. All raw files were demultiplexed for FAIMS CVs using the Coons lab "FAIMS to Mzxml generator" (https://github.com/coongroup/FAIMS-MzXML-Generator). Mzxml files were analyzed with MaxQuant 1.6.14.0 using a Uniprot mouse protein database (release July 3, 2020). Default settings were used plus: Multiplicity set to 2, label: lys6, enzyme: LysC/P, p(STY) enabled as variable modification, a match between runs was enabled, unmodified counterpart peptides were not discarded. The resulting MaxQuant (Tyanova *et al*, 2015) output was further analyzed in Perseus 1.6.14.0 (Cox & Mann, 2012) and InstantClue 0.10.10 (Nolte *et al*, 2018).

Immunoprecipitation of PKA substrates

WT brains were homogenized in Co-IP buffer and processed as described above. A total amount of 2 mg protein was provided to the beads. The samples were loaded onto an SDS-PAGE gel and sample preparation followed in-gel digestion protocol (described above). Eluted peptides were dried in vacuo, resuspended in 1% formic acid/4% acetonitrile and stored at −20°C prior MS measurement. All samples were analyzed on a Q Exactive Plus Orbitrap mass spectrometer that was coupled to an EASY nLC (both Thermo Scientific). Peptides were loaded with solvent A (0.1% formic acid in water) onto an in-house packed analytical column (50 cm, 75 μm I.D., filled with 2.7 μm Poroshell EC120 C18, Agilent). Peptides were chromatographically separated at a constant flow rate of 250 nl/min using the following gradient: 3–5% solvent B (0.1% formic acid in 80% acetonitrile) within 1.0 min, 5–30% solvent B within 40.0 min, 30–50% solvent B within 8.0 min, 50–95% solvent B within 1.0 min, followed by washing and column equilibration. The mass spectrometer was operated in data-dependent acquisition mode. The MS1 survey scan was acquired from 300–1,750 m/z at a resolution of 70,000. The top 10 most abundant peptides were isolated within a 1.8 Th window and subjected to HCD fragmentation at a normalized collision energy of 27%. The AGC target was set to 5e5 charges, allowing a maximum injection time of 110 ms. Product ions were detected in the Orbitrap at a resolution of 35,000. Precursors were dynamically excluded for 10.0 s. All mass spectrometric raw data were processed with Maxquant (version 1.5.3.8) using default parameters. Briefly, MS2 spectra were searched against the Uniprot mouse reference proteome containing isoforms (UP000000589, downloaded on 26.08.2020), including a list of common contaminants. False discovery rates on protein and PSM levels were estimated by the target-decoy approach at 1% (Protein FDR) and 1% (PSM FDR) respectively. The minimal peptide length was set to 7 amino acids and carbamidomethylation at cysteine residues was considered as a fixed modification. Oxidation (M), Phospho (STY), and Acetyl (Protein N-term) were included as variable modifications. The match-between runs option was enabled. LFQ quantification was enabled using default settings.

Pathway analysis

Pathway analysis of proteomic approaches was performed using WebGestalt (WEB-based GEne SeT AnaLysis Toolkit, developed and maintained by the Zhang Lab, Baylor College of Medicine, Houston, Texas) and ShinyGO v0.741: Gene Ontology Enrichment Analysis

(http://bioinformatics.sdstate.edu/go/). Venn diagrams were created using Gene List Venn Diagram, an interactive tool for comparing lists with Venn's diagrams (http://genevenn.sourceforge.net/). GO functional analysis and human phenotype ontology analysis were done using g:Profiler (https://biit.cs.ut.ee/gprofiler/gost).

Statistical analyses

Sample sizes were not chosen based on pre-specified effect size. Instead, multiple independent experiments were carried out using several samples replicates as detailed in the figure legends. For all experiments, there was enough statistical power to detect the corresponding effect size. Statistical analyses were done on cell values (indicated by data points) from at least three independent experiments (indicated by "n", biological replicates) with the exception of Fig 6M. MS Excel (Microsoft, USA) and GraphPad Prism version 9 (GraphPad Software, Inc., USA) were used statistical analysis and result illustration (unless otherwise stated). Statistical analysis of normalized data between the two groups was performed using a one-tailed unpaired Student's *t*-test. Statistical significance between two groups for normally distributed non-normalized data was evaluated with a two-tailed unpaired Student's *t*-test. Two-tailed unpaired Mann-Whitney test was used for analysis between two groups for non-normally distributed non-normalized data (i.e. SHIRPA analysis). Statistical difference between more than two groups and two conditions was evaluated using Two-Way ANOVA (Tukey posthoc test was used to determine the statistical significance between the groups). Statistical difference between more than two groups was calculated using One-way ANOVA with Dunnett's multiple comparison test. One-way ANOVA with Dunn's multiple comparison (Kruskal-Wallis test) was used for comparison between more than two groups for not normally distributed data. ROUT-based outlier analysis was applied to data sets before statistical analysis. Immunofluorescence data collection was not blinded because of the strong accumulation of PKA R1 in KO. Western blot data were analyzed in a non-blinded fashion as KO proteins were assessed for each experiment. A normality test using GraphPad Prism version 9 (Shapiro-Wilk test) was performed to determine the parametric and nonparametric statistical tests used for analysis (for data sets with > 8 data points). Data were excluded only when sample quality was not optimal and/or due to re-genotyping results (p62-WB analysis was used when re-genotyping was not possible). Predefined quality criteria were: in living samples-vacuolization or other signs of cellular degeneration, normal cell morphology and protein transport (which is usually hampered in unhealthy cells) and image streams that are in focus; proper sample preparation and mounting in fixed samples. Significant differences were accepted at $P < 0.05$ indicated by asterisks: *$P < 0.05$; **$P < 0.01$; ***$P < 0.001$.

Data availability

All used materials are commercially available. All data supporting the findings described in this study are available from the corresponding author upon reasonable request. Source data from all representative blots shown in this study as well as data underlying all quantitative analysis performed in this study are provided with the manuscript as a Source Data file. The full Kallisto-based transcriptome analysis is presented in Dataset EV2. Mass spectrometry data

have been deposited in the ProteomeXchange Consortium via the PRIDE (PubMed ID: 26527722) partner repository with the following dataset identifier:

Project name	Figure	Project accession
Proteome and phosphoproteome analysis of autophagy-deficient ATG5flox:CamKII-Cre and ATG5flox:*Slc32a* -Cre conditional knockout mice	Fig 2A,B Fig 6C	PXD029435
Global proteome of Atg5flox:CamKIIα-Cre:tdTomato FACS sorted WT and KO neurons	Fig 2C	PXD031552
Global proteome of Atg5flox:Slc32a1-Cre:tdTomato FACS sorted WT and KO neurons	Fig 2D	PXD031535
Global proteome of *Atg5*flox:*CAG*-Cre^Tmx WT and KO neurons	Appendix Fig S4J	PXD031487
Global proteome of Atg16L1flox:CAG-CreTmx WT and KO neurons	Appendix Fig S4M	PXD031555
Detection of putative PKA target phosphorylation sites in Atg5flox:CamKII-Cre WT and KO acute brain slices	Fig 7E Appendix Fig S8C	PXD031106

Expanded View for this article is available online.

Acknowledgements

Author contributions

Melina Overhoff: Conceptualization; data curation; formal analysis; investigation; writing—original draft; writing—review and editing. **Frederik Telkamp:** Data curation; formal analysis; investigation; methodology. **Simon Hess:** Data curation; formal analysis; investigation; methodology. **Marianna Tolve:** Data curation. **Janine Tutas:** Data curation. **Marcel Faerfers:** Data curation; formal analysis. **Lotte Ickert:** Data curation; formal analysis. **Milad Mohammadi:** Data curation; formal analysis. **Elodie De Bruyckere:** Data curation; formal analysis; investigation. **Emmanouela Kallergi:** Data curation; formal analysis; investigation; methodology. **Andrea Delle Vedove:** Resources; formal analysis; methodology. **Vassiliki Nikoletopoulou:** Data curation; formal analysis; investigation; methodology. **Brunhilde Wirth:** Resources; supervision. **Joerg Isensee:** Resources. **Tim Hucho:** Resources; methodology. **Dmytro Puchkov:** Data curation; formal analysis; methodology. **Dirk Isbrandt:** Data curation; formal analysis; methodology. **Marcus Krueger:** Supervision; methodology. **Peter Kloppenburg:** Supervision; methodology. **Natalia L Kononenko:** Conceptualization; data curation; formal analysis; supervision; funding acquisition; investigation; methodology; writing—original draft; project administration; writing—review and editing.

Disclosure and competing interests statement

The authors declare that they have no conflict of interest.

References

Abel T, Nguyen PV (2008) Regulation of hippocampus-dependent memory by cyclic AMP-dependent protein kinase. *Prog Brain Res* 169: 97–115

Andres-Alonso M, Ammar MR, Butnaru I, Gomes GM, Acuña Sanhueza G, Raman R, Yuanxiang P, Borgmeyer M, Lopez-Rojas J, Raza SA *et al* (2019) SIPA1L2 controls trafficking and local signaling of TrkB-containing amphisomes at presynaptic terminals. *Nat Commun* 10: 5448

Ashrafi G, Schlehe JS, LaVoie MJ, Schwarz TL (2014) Mitophagy of damaged mitochondria occurs locally in distal neuronal axons and requires PINK1 and parkin. *J Cell Biol* 206: 655–670

Bączyk M, Alami NO, Delestrée N, Martinot C, Tang L, Commisso B, Bayer D, Doisne N, Frankel W, Manuel M *et al* (2020) Synaptic restoration by cAMP/PKA drives activity-dependent neuroprotection to motoneurons in ALS. *J Exp Med* 217: e20191734

Barker-Haliski M, White HS (2015) Glutamatergic mechanisms associated with seizures and epilepsy. *Cold Spring Harb Perspect Med* 5: a022863

Besag FM (2017) Epilepsy in patients with autism: links, risks and treatment challenges. *Neuropsychiatr Dis Treat* 14: 1–10

Bhukel A, Beuschel CB, Maglione M, Lehmann M, Juhász G, Madeo F, Sigrist SJ (2019) Autophagy within the mushroom body protects from synapse aging in a non-cell autonomous manner. *Nat Commun* 10: 1318

Bray NL, Pimentel H, Melsted P, Pachter L (2016) Near-optimal probabilistic RNA-seq quantification. *Nat Biotechnol* 34: 525–527

Bruderer R, Bernhardt OM, Gandhi T, Miladinović SM, Cheng L-Y, Messner S, Ehrenberger T, Zanotelli V, Butscheid Y, Escher C *et al* (2015) Extending the limits of quantitative proteome profiling with data-independent acquisition and application to acetaminophen-treated three-dimensional liver microtissues. *Mol Cell Proteomics* 14: 1400–1410

Carroll RC, Beattie EC, Xia H, Lüscher C, Altschuler Y, Nicoll RA, Malenka RC, von Zastrow M (1999) Dynamin-dependent endocytosis of ionotropic glutamate receptors. *Proc Natl Acad Sci USA* 96: 14112–14117

Chain DG, Casadio A, Schacher S, Hegde AN, Valbrun M, Yamamoto N, Goldberg AL, Bartsch D, Kandel ER, Schwartz JH (1999) Mechanisms for

generating the autonomous cAMP-dependent protein kinase required for long-term facilitation in Aplysia. *Neuron* 22: 147–156

Cherra SJ 3rd, Kulich SM, Uechi G, Balasubramani M, Mountzouris J, Day BW, Chu CT (2010) Regulation of the autophagy protein LC3 by phosphorylation. *J Cell Biol* 190: 533–539

Cho RW, Buhl LK, Volfson D, Tran A, Li F, Akbergenova Y, Littleton JT (2015) Phosphorylation of Complexin by PKA regulates activity-dependent spontaneous neurotransmitter release and structural synaptic plasticity. *Neuron* 88: 749–761

Chowdhury D, Hell JW (2018) Homeostatic synaptic scaling: molecular regulators of synaptic AMPA-type glutamate receptors. *F1000Res* 7: 234

Chua JP, De Calbiac H, Kabashi E, Barmada SJ (2021) Autophagy and ALS: mechanistic insights and therapeutic implications. *Autophagy* 18: 254–282

Compans B, Camus C, Kallergi E, Sposini S, Martineau M, Butler C, Kechkar A, Klaassen RV, Retailleau N, Sejnowski TJ *et al* (2021) NMDAR-dependent long-term depression is associated with increased short term plasticity through autophagy mediated loss of PSD-95. *Nat Commun* 12: 2849

Cox J, Mann M (2012) 1D and 2D annotation enrichment: a statistical method integrating quantitative proteomics with complementary high-throughput data. *BMC Bioinformatics* 13(Suppl 16): S12

D'Andrea Meira I, Romão TT, Pires do Prado HJ, Krüger LT, Pires MEP, da Conceição PO (2019) Ketogenic diet and epilepsy: what we know so far. *Front Neurosci* 13: 5

Day ME, Gaietta GM, Sastri M, Koller A, Mackey MR, Scott JD, Perkins GA, Ellisman MH, Taylor SS (2011) Isoform-specific targeting of PKA to multivesicular bodies. *J Cell Biol* 193: 347–363

Demichev V, Messner CB, Vernardis SI, Lilley KS, Ralser M (2020) DIA-NN: neural networks and interference correction enable deep proteome coverage in high throughput. *Nat Methods* 17: 41–44

Deng Z, Li X, Blanca Ramirez M, Purtell K, Choi I, Lu J-H, Yu Q, Yue Z (2021) Selective autophagy of AKAP11 activates cAMP/PKA to fuel mitochondrial metabolism and tumor cell growth. *Proc Natl Acad Sci USA* 118: e2020215118

Desch K, Langer JD, Schuman EM (2021) Dynamic bi-directional phosphorylation events associated with the reciprocal regulation of synapses during homeostatic up- and down-scaling. *Cell Rep* 36: 109583

Dikic I, Elazar Z (2018) Mechanism and medical implications of mammalian autophagy. *Nat Rev Mol Cell Biol* 19: 349–364

Esteban JA, Shi S-H, Wilson C, Nuriya M, Huganir RL, Malinow R (2003) PKA phosphorylation of AMPA receptor subunits controls synaptic trafficking underlying plasticity. *Nat Neurosci* 6: 136–143

Gessulat S, Schmidt T, Zolg DP, Samaras P, Schnatbaum K, Zerweck J, Knaute T, Rechenberger J, Delanghe B, Huhmer A *et al* (2019) Prosit: Proteome-wide prediction of peptide tandem mass spectra by deep learning. *Nat Methods* 16: 509–518

Glatigny M, Moriceau S, Rivagorda M, Ramos-Brossier M, Nascimbeni AC, Lante F, Shanley MR, Boudarene N, Rousseaud A, Friedman AK *et al* (2019) Autophagy is required for memory formation and reverses age-related memory decline. *Curr Biol* 29: 435–448.e438

Goldsmith J, Ordureau A, Harper JW, Holzbaur ELF (2022) Brain-derived autophagosome profiling reveals the engulfment of nucleoid-enriched mitochondrial fragments by basal autophagy in neurons. *Neuron* 110: 967–976.e8

Greengard P, Jen J, Nairn AC, Stevens CF (1991) Enhancement of the glutamate response by cAMP-dependent protein kinase in hippocampal neurons. *Science* 253: 1135–1138

Guo C, Ma Y-Y (2021) Calcium permeable-AMPA receptors and excitotoxicity in neurological disorders. *Front Neural Circuits* 15: 711564

Han S, Jeong YY, Sheshadri P, Su X, Cai Q (2020) Mitophagy regulates integrity of mitochondria at synapses and is critical for synaptic maintenance. *EMBO Rep* 21: e49801

Hatcher JP, Jones DN, Rogers DC, Hatcher PD, Reavill C, Hagan JJ, Hunter AJ (2001) Development of SHIRPA to characterise the phenotype of gene-targeted mice. *Behau Brain Res* 125: 43–47

Hernandez D, Torres Ciara A, Setlik W, Cebrián C, Mosharov Eugene V, Tang G, Cheng H-C, Kholodilov N, Yarygina O, Burke Robert E *et al* (2012) Regulation of presynaptic neurotransmission by macroautophagy. *Neuron* 74: 277–284

Hilfiker S, Czernik AJ, Greengard P, Augustine GJ (2001) Tonically active protein kinase a regulates neurotransmitter release at the squid giant synapse. *J Physiol* 531: 141–146

Hoffmann S, Orlando M, Andrzejak E, Bruns C, Trimbuch T, Rosenmund C, Garner CC, Ackermann F (2019) Light-activated ROS production induces synaptic autophagy. *J Neurosci* 39: 2163–2183

Hoffmann-Conaway S, Brockmann MM, Schneider K, Annamneedi A, Rahman KA, Bruns C, Textoris-Taube K, Trimbuch T, Smalla K-H, Rosenmund C *et al* (2020) Parkin contributes to synaptic vesicle autophagy in bassoon-deficient mice. *Elife* 9: e56590

Huber W, Carey VJ, Gentleman R, Anders S, Carlson M, Carvalho BS, Bravo HC, Davis S, Gatto L, Girke T *et al* (2015) Orchestrating high-throughput genomic analysis with Bioconductor. *Nat Methods* 12: 115–121

Hughes CS, Moggridge S, Müller T, Sorensen PH, Morin GB, Krijgsveld J (2019) Single-pot, solid-phase-enhanced sample preparation for proteomics experiments. *Nat Protoc* 14: 68–85

Ilouz R, Bubis J, Wu J, Yim YY, Deal MS, Kornev AP, Ma Y, Blumenthal DK, Taylor SS (2012) Localization and quaternary structure of the PKA RIβ holoenzyme. *Proc Natl Acad Sci USA* 109: 12443–12448

Jonas P, Burnashev N (1995) Molecular mechanisms controlling calcium entry through AMPA-type glutamate receptor channels. *Neuron* 15: 987–990

Joshi S, Kapur J (2018) Mechanisms of status epilepticus: α-Amino-3-hydroxy-5-methyl-4-isoxazolepropionic acid receptor hypothesis. *Epilepsia* 59 Suppl 2: 78–81

Kiral FR, Linneweber GA, Mathejczyk T, Georgiev SV, Wernet MF, Hassan BA, von Kleist M, Hiesinger PR (2020) Autophagy-dependent filopodial kinetics restrict synaptic partner choice during drosophila brain wiring. *Nat Commun* 11: 1325

Koh YH, Popova E, Thomas U, Griffith LC, Budnik V (1999) Regulation of DLG localization at synapses by CaMKII-dependent phosphorylation. *Cell* 98: 353–363

Kononenko NL, Diril MK, Puchkov D, Kintscher M, Koo SJ, Pfuhl G, Winter Y, Wienisch M, Klingauf J, Breustedt J *et al* (2013) Compromised fidelity of endocytic synaptic vesicle protein sorting in the absence of stonin 2. *Proc Natl Acad Sci USA* 110: E526–E535

Kononenko NL, Claßen GA, Kuijpers M, Puchkov D, Maritzen T, Tempes A, Malik AR, Skalecka A, Bera S, Jaworski J *et al* (2017) Retrograde transport of TrkB-containing autophagosomes via the adaptor AP-2 mediates neuronal complexity and prevents neurodegeneration. *Nat Commun* 8: 1–16

Krüger M, Moser M, Ussar S, Thievessen I, Luber CA, Forner F, Schmidt S, Zanivan S, Fässler R, Mann M (2008) SILAC mouse for quantitative proteomics uncovers Kindlin-3 as an essential factor for red blood cell function. *Cell* 134: 353–364

Kuijpers M, Kochlamazashvili G, Stumpf A, Puchkov D, Swaminathan A, Lucht MT, Krause E, Maritzen T, Schmitz D, Haucke V (2021) Neuronal autophagy regulates presynaptic neurotransmission by controlling the axonal endoplasmic reticulum. *Neuron* 109: e299

Lalonde R, Filali M, Strazielle C (2021) SHIRPA as a neurological screening battery in mice. *Curr Protoc* 1: e135

Lee HK, Takamiya K, Han JS, Man H, Kim CH, Rumbaugh G, Yu S, Ding L, He C, Petralia RS *et al* (2003) Phosphorylation of the AMPA receptor GluR1 subunit is required for synaptic plasticity and retention of spatial memory. *Cell* 112: 631–643

Lee S, Sato Y, Nixon RA (2011) Lysosomal proteolysis inhibition selectively disrupts axonal transport of degradative organelles and causes an Alzheimer's-like axonal dystrophy. *J Neurosci* 31: 7817–7830

Lee K-M, Hwang S-K, Lee J-A (2013) Neuronal autophagy and neurodevelopmental disorders. *Exp Neurobiol* 22: 133–142

Leonard AS, Davare MA, Horne MC, Garner CC, Hell JW (1998) SAP97 is associated with the alpha-amino-3-hydroxy-5-methylisoxazole-4-propionic acid receptor GluR1 subunit. *J Biol Chem* 273: 19518–19524

Lüningschrör P, Binotti B, Dombert B, Heimann P, Perez-Lara A, Slotta C, Thau-Habermann N. R., von Collenberg C, Karl F, Damme M *et al* (2017) Plekhg5-regulated autophagy of synaptic vesicles reveals a pathogenic mechanism in motoneuron disease. *Nat Commun* 8: 678

Maday S, Holzbaur ELF (2016) Compartment-specific regulation of autophagy in primary neurons. *J Neurosci* 36: 5933–5945

Maday S, Holzbaur Erika LF (2014) Autophagosome biogenesis in primary neurons follows an ordered and spatially regulated pathway. *Dev Cell* 30: 71–85

Mariottini C, Munari L, Gunzel E, Seco JM, Tzavaras N, Hansen J, Stern SA, Gao V, Aleyasin H, Sharma A *et al* (2019) Wilm's tumor 1 promotes memory flexibility. *Nat Commun* 10: 3756

Martin M (2011) Cutadapt removes adapter sequences from high-throughput sequencing reads. *EMBnet.journal* 17: 10

Mavrakis M, Lippincott-Schwartz J, Stratakis CA, Bossis I (2006) Depletion of type IA regulatory subunit (RIα) of protein kinase a (PKA) in mammalian cells and tissues activates mTOR and causes autophagic deficiency. *Hum Mol Genet* 15: 2962–2971

McMahon J, Huang X, Yang J, Komatsu M, Yue Z, Qian J, Zhu X, Huang Y (2012) Impaired autophagy in neurons after disinhibition of mammalian target of rapamycin and its contribution to Epileptogenesis. *J Neurosci* 32: 15704–15714

Menzies FM, Fleming A, Caricasole A, Bento CF, Andrews SP, Ashkenazi A, Fullgrabe J, Jackson A, Jimenez Sanchez M, Karabiyik C *et al* (2017) Autophagy and neurodegeneration: pathogenic mechanisms and therapeutic opportunities. *Neuron* 93: 1015–1034

Mizushima N, Yamamoto A, Matsui M, Yoshimori T, Ohsumi Y (2004) In vivo analysis of autophagy in response to nutrient starvation using transgenic mice expressing a fluorescent autophagosome marker. *Mol Biol Cell* 15: 1101–1111

Negrete-Hurtado A, Overhoff M, Bera S, De Bruyckere E, Schätzmüller K, Kye MJ, Qin C, Lammers M, Kondylis V, Neundorf I *et al* (2020) Autophagy lipidation machinery regulates axonal microtubule dynamics but is dispensable for survival of mammalian neurons. *Nat Commun* 11: 1535

Nikoletopoulou V, Sidiropoulou K, Kallergi E, Dalezios Y, Tavernarakis N (2017) Modulation of autophagy by BDNF underlies synaptic plasticity. *Cell Metab* 26: 230–242.e235

Nolte H, MacVicar TD, Tellkamp F, Krüger M (2018) Instant clue: a software suite for interactive data visualization and analysis. *Sci Rep* 8: 12648

Okerlund ND, Schneider K, Leal-Ortiz S, Montenegro-Venegas C, Kim SA, Garner LC, Waites CL, Gundelfinger ED, Reimer RJ, Garner CC (2018) Bassoon controls presynaptic autophagy through Atg5. *Neuron* 97: 727

Overhoff M, De Bruyckere E, Kononenko NL (2021) Mechanisms of neuronal survival safeguarded by endocytosis and autophagy. *J Neurochem* 157: 263–296

Pandey K, Yu XW, Steinmetz A, Alberini CM (2021) Autophagy coupled to translation is required for long-term memory. *Autophagy* 17: 1614–1635

Pimentel H, Bray NL, Puente S, Melsted P, Pachter L (2017) Differential analysis of RNA-seq incorporating quantification uncertainty. *Nat Methods* 14: 687–690

Scrivo A, Bourdenx M, Pampliega O, Cuervo AM (2018) Selective autophagy as a potential therapeutic target for neurodegenerative disorders. *Lancet Neurol* 17: 802–815

Searle BC, Pino LK, Egertson JD, Ting YS, Lawrence RT, MacLean BX, Villén J, MacCoss MJ (2018) Chromatogram libraries improve peptide detection and quantification by data independent acquisition mass spectrometry. *Nat Commun* 9: 5128

Searle BC, Swearingen KE, Barnes CA, Schmidt T, Gessulat S, Küster B, Wilhelm M (2020) Generating high quality libraries for DIA MS with empirically corrected peptide predictions. *Nat Commun* 11: 1548

Shabb JB (2001) Physiological substrates of cAMP-dependent protein kinase. *Chem Rev* 101: 2381–2411

Shehata M, Matsumura H, Okubo-Suzuki R, Ohkawa N, Inokuchi K (2012) Neuronal stimulation induces autophagy in hippocampal neurons that is involved in AMPA receptor degradation after chemical long-term depression. *J Neurosci* 32: 10413

Shen W, Ganetzky B (2009) Autophagy promotes synapse development in drosophila. *J Cell Biol* 187: 71–79

Shen L, Liang F, Walensky LD, Huganir RL (2000) Regulation of AMPA receptor GluR1 subunit surface expression by a 4. 1N-linked Actin cytoskeletal association. *J Neurosci* 20: 7932–7940

Shen H, Zhu H, Panja D, Gu Q, Li Z (2020a) Autophagy controls the induction and developmental decline of NMDAR-LTD through endocytic recycling. *Nat Commun* 11: 2979

Shen W, Kilander MBC, Bridi MS, Frei JA, Niescier RF, Huang S, Lin YC (2020b) Tomosyn regulates the small RhoA GTPase to control the dendritic stability of neurons and the surface expression of AMPA receptors. *J Neurosci Res* 98: 1213–1231

Smith KR, Kopeikina KJ, Fawcett-Patel JM, Leaderbrand K, Gao R, Schürmann B, Myczek K, Radulovic J, Swanson GT, Penzes P (2014) Psychiatric risk factor ANK3/ankyrin-G nanodomains regulate the structure and function of glutamatergic synapses. *Neuron* 84: 399–415

Stavoe Andrea KH, Hill Sarah E, Hall David H, Colón-Ramos Daniel A (2016) KIF1A/UNC-104 transports ATG-9 to regulate neurodevelopment and autophagy at synapses. *Dev Cell* 38: 171–185

Takumi Y, Ramírez-León V, Laake P, Rinvik E, Ottersen OP (1999) Different modes of expression of AMPA and NMDA receptors in hippocampal synapses. *Nat Neurosci* 2: 618–624

Tang S, Yasuda R (2017) Imaging ERK and PKA activation in single dendritic spines during structural plasticity. *Neuron* 93: 1315–1324.e1313

Tang G, Gudsnuk K, Kuo S-H, Cotrina Marisa L, Rosoklija G, Sosunov A, Sonders Mark S, Kanter E, Castagna C, Yamamoto A *et al* (2014) Loss of mTOR-dependent macroautophagy causes autistic-like synaptic pruning deficits. *Neuron* 83: 1131–1143

Tao-Cheng J-H (2019) Stimulation induces gradual increases in the thickness and curvature of postsynaptic density of hippocampal CA1 neurons in slice cultures. *Mol Brain* 12: 44

Tatavarty V, Torrado Pacheco A, Groves Kuhnle C, Lin H, Koundinya P, Miska NJ, Hengen KB, Wagner FF, Van Hooser SD, Turrigiano GG (2020) Autism-

associated Shank3 is essential for homeostatic compensation in rodent V1. *Neuron* 106: 769−777.e764

Tavalin SJ, Colledge M, Hell JW, Langeberg LK, Huganir RL, Scott JD (2002) Regulation of GluR1 by the A-kinase anchoring protein 79 (AKAP79) signaling complex shares properties with long-term depression. *J Neurosci* 22: 3044

Taylor SS, Wu J, Bruystens JGH, Del Rio JC, Lu T-W, Kornev AP, Ten Eyck LF (2021) From structure to the dynamic regulation of a molecular switch: a journey over 3 decades. *J Biol Chem* 296: 100746

Tsvetkov AS, Mitra S, Finkbeiner S (2009) Protein turnover differences between neurons and other cells. *Autophagy* 5: 1037−1038

Tyanova S, Temu T, Carlson A, Sinitcyn P, Mann M, Cox J (2015) Visualization of LC-MS/MS proteomics data in MaxQuant. *Proteomics* 15: 1453−1456

Tyanova S, Temu T, Sinitcyn P, Carlson A, Hein MY, Geiger T, Mann M, Cox J (2016) The Perseus computational platform for comprehensive analysis of (prote)omics data. *Nat Methods* 13: 731−740

Uchino S, Wada H, Honda S, Nakamura Y, Ondo Y, Uchiyama T, Tsutsumi M, Suzuki E, Hirasawa T, Kohsaka S (2006) Direct interaction of post-synaptic density-95/Dlg/ZO-1 domain-containing synaptic molecule Shank3 with GluR1 alpha-amino-3-hydroxy-5-methyl-4-isoxazole propionic acid receptor. *J Neurochem* 97: 1203−1214

Wang Y, Yuan J, Yu X, Liu X, Tan C, Chen Y, Xu T (2021) Vezatin regulates seizures by controlling AMPAR-mediated synaptic activity. *Cell Death Dis* 12: 936

Wu LJ, Ren M, Wang H, Kim SS, Cao X, Zhuo M (2008) Neurabin contributes to hippocampal long-term potentiation and contextual fear memory. *PLoS One* 3: e1407

Ye JH, Zhang J, Xiao C, Kong J-Q (2006) Patch-clamp studies in the CNS illustrate a simple new method for obtaining viable neurons in rat brain slices: glycerol replacement of NaCl protects CNS neurons. *J Neurosci Methods* 158: 251−259

Young JE, Martinez RA, La Spada AR (2009) Nutrient deprivation induces neuronal autophagy and implicates reduced insulin signaling in neuroprotective autophagy activation. *J Biol Chem* 284: 2363−2373

Zhang J, Li J, Yin Y, Li X, Jiang Y, Wang Y, Cha C, Guo G (2020) Collapsin response mediator protein 2 and Endophilin2 coordinate regulation of AMPA receptor GluA1 subunit recycling. *Front Mol Neurosci* 13: 128

Zhao X, Nedvetsky P, Stanchi F, Vion A-C, Popp O, Zühlke K, Dittmar G, Klussmann E, Gerhardt H (2019) Endothelial PKA activity regulates angiogenesis by limiting autophagy through phosphorylation of ATG16L1. *Elife* 8: e46380